UNIVERSITY OF CALIFORNIA
RIVERSIDE

# Structural and Functional Characterizations of Flavivirus NS5: Perspective for Drug Discovery and Vaccine Development

A Dissertation submitted in partial satisfaction
of the requirements for the degree of

Doctor of Philosophy

in

Biochemistry and Molecular Biology

by

Boxiao Wang

June 2020

Dissertation Committee:

Dr. Jikui Song, Chairperson
Dr. Rong Hai
Dr. Gregor Blaha

The Dissertation of Boxiao Wang is approved:

_____

_____

_____

Committee Chairperson

University of California, Riverside

ACKNOWLEDGEMENTS

The text of this dissertation, in part or in full, is a reprint of the material as it appears in:

1. Wang B*, Tan X*, Thurmond S, Zhang ZM, Lin A, Hai R, Song J. (2017). The structure of Zika virus NS5 reveals a conserved domain conformation[J]. Nature communications, 2017, 8: 14763

2. Wang B*, Thurmond S, Hai R, Song J. Structure and function of Zika virus NS5 protein: perspectives for drug design[J]. Cellular and molecular life sciences, 2018, 75(10): 1723-1736.

3. Thurmond S, Wang B, Song J, Rong H. Suppression of type I interferon signaling by flavivirus NS5[J]. Viruses, 2018, 10(12): 712.

4. Wang B*, Thurmond S*, Zhou K*, Sánchez-Aparicio M*, Fang J, Lu J, Gao L, Ren W, Cui Y, Veit E, Hong H, Evans M, O'Leary S, García-Sastre A, Zhou ZH, Hai R, Song J. Structural basis for STAT2 suppression by flavivirus NS5. Manuscript under review by Nature Structural & Molecular Biology.

*: These authors contribute equally to this work.

The co-author Dr. Jikui Song listed in those publications directed and supervised the research which forms the basis for this dissertation.

ABSTRACT OF THE DISSERTATION

Structural and Functional Characterizations of Flavivirus NS5: Perspective for Drug Discovery and Vaccine Development

by

Boxiao Wang

Doctor of Philosophy, Graduate Program in Biochemistry and Molecular Biology
University of California, Riverside, June 2020
Dr. Jikui Song, Chairperson

Flaviviruses have historically caused severe epidemics or pandemics, but few therapies are available currently. NS5 is a critical enzyme responsible for flaviviral life cycle, and suppresses host immune response via host-pathogen interaction as well. In this study, we determined the crystal structure of Zika virus (ZIKV), a member of flavivirus family, revealing flavivirus NS5 proteins share a conserved domain conformation. A small molecule inhibitor, I29, was subsequently proved to bind to ZIKV NS5. Meanwhile, we solved the structure of ZIKV NS5 in complex with its host partner, human STAT2 (hSTAT2), suggesting a bypass pathway to interfere immune response. We were able to rescue viral strains with mutations of residues involved in hSTAT2-binding, providing novel insights into vaccine development.

## Table of Contents

## List of Figures

## List of Tables

## Introduction

### 1. Flaviviruses are global health concerns

Flaviviruses are a type of arthropod-borne RNA virus, including Zika Virus (ZIKV), Dengue Virus (DENV), West Nile Virus (WNV), Japanese Encephalitis Virus (JEV), etc., have caused a great number of global disease outbreaks. Infection of flavivirus would lead to a broad range of symptoms from mild ones like fever, headache or joint pain to severe ones like birth defect, nervous system damage or even fatally hemorrhagic fever. Flavivirus belongs to the Flaviviradae family which consists of three genera, hepacivirus, pestivirus and flavivirus, of particular note is hepatitis C virus (HCV), which is a member of flaviviradae and could lead to severe liver disease. As arthropod, especially mosquito, being the primary vector, the transmission of some flaviviruses are prone to have seasonal patterns owing to the climate-driven outbreaks of mosquito, constantly threatening the global health[1]. Despite the significant risk posed by flavivirus, there are no antiviral therapies and only limited vaccines so far. A comprehensive understanding of the molecular basis underpinning the viral life cycle and host-pathogen interaction is therefore indispensable for available treatments.

### 2. Flaviviral life cycle

*Flavivirus* genomes are ~11 kb single positive strand RNA molecules flanked by 5'

UTR and 3' UTR. After entering host cells, the viral genome will be translated into a single polyprotein chain which can further be proteolytically processed into three structural proteins (C, prM/M and E) and seven non-structural (NS) proteins (NS1, NS2A, NS2B, NS3, NS4A, NS4B and NS5). To efficiently produce new viral genomes, NS proteins are gathered to form the replication complex (RC), with NS5 possessing RNA polymerase activity for RNA replication and methyltransferase activity for capping neosythesized viral genome, NS3 containing a helicase domain for unwinding the double-stranded RNA and a triphosphate responsible for RNA capping, NS1 associating the RC to ER membranes, and the rest of NS proteins either acting as cofactors or being involved in membrane alterations[2]. The neosynthesized viral RNA is then encapsidated into viral particles formed by structural proteins, resulting in the assembled viruses being transmitted from ER to Golgi apparatus for the release of infectious virions[3].

## 3. NS5 plays a critical role in flaviviral life cycle

NS5 is the largest and most conserved protein among all NS members. It has an N-terminal methylltransferase (MTase) domain and a C-terminal RNA-dependent RNA polymerase (RdRp) domain.

### 3.1 RdRp performs a *de novo* RNA replication

The RdRp domain synthesizes viral RNA in a primer-independent manner termed "*de*

*novo* RNA replication"[4-6]. Three subdomains, Palm, Thumb and Fingers, are the basic components of RdRp and engaged in processing this replication mode. Upon initiation of viral genome replication, a dinucleotide primer, $_{ppp}$AG, has to be generated first for pairing with a strictly conserved CU sequence at the 3' end of template, the polymerase then undergoes a conformational change from an initiation phase to an elongation phase, subsequently triggering the processive RNA polymerization[4,7,8]. Structural and biochemical studies of hepatitis C virus (HCV) RdRp which is a counterpart of flavivirus RdRp highlights the critical role of a flexible region in phase transition: this linker region inserted in Thumb subdomain, named "priming loop", protrudes to block the active site in apo state, while retracts in the polymerase : template : dinucleotide primer ternary complex, generating more space for RNA-binding[9,10]. Furthermore, the crystallization of an RdRp-RNA complex mimicking the elongation phase has to be exclusive of intact priming loop and the crystal structures display a further distance between Thumb and the other two subdomains, suggesting the absence of priming loop and a more RNA-accommodated conformation when polymerizing nascent strand[9]. Besides the CU sequence initiating RNA replication by Watson-Crick base pairs with dinucleotide primer, the highly structured 5' UTR and 3' UTR of flaviviral genome are also essential for RNA replication. On one hand, there are two adjacent stem-loop structures resided within the 3' UTR, which are conserved among flaviviruses[11-14]. These two regions, collectively

termed "3' SL", are critical for producing minus strand and binds host cellular proteins for enhancing RNA replication[15-17]. In addition, 3' SL is capable of interacting with NS5 and NS3, suggesting this region might promote the formation of replication complex[18]. On the other hand, 5' UTR contains two stem-loop regions: a large stem loop A (SLA) and a short stem loop B (SLB) [19,20]. SLA was found to fold into a Y-shaped structure and serve as a promoter of RdRp activity[21,22], whereas SLB encompasses a 5' upstream AUG region (5' UAR) to promote the genome cyclization which is necessary for viral replication[23,24]. Collectively, the specific structures of flaviviral genome are critical to the *de novo* RNA replication,

### 3.2 MTase is responsible for capping viral genome

In spite of three *Flaviviradae* genera sharing similar genome constructions, a cap structure in the 5' UTR is only required to flavivirus life cycle. It turns out that flaviviral NS5 proteins display an unique conformation where a methyltransferase domain locates on the N-terminus. In accordance with the previous studies of a wide range of animal viruses, it is most likely that the cap modification is involved in the progress of pre-mRNA processing and the translation of mature mRNA, enables the nucleus shuttling of viral genome and prevents viral RNA from the degradation by host immune system[25]. Previous biochemical and kinetic studies suggested four steps to get involved in the methylation reaction: (1) The NS3 triphosphate removes the 5′-γ-phosphate of the nascent

genome[26,27], (2) The MTase domain exerts the guanyltransferase (GTase) activity to catalyze a guanosine monophosphate (GMP) onto the 5' end via a phosphodiester bond linkage, the so called "capping"[28,29], (3) The MTase then transfers the methyl group to the N7 site of guanine moiety, resulting in a second-methylation-favored substrate [30,31], (4) The methyltransferase carries out the second methylation reaction at the ribose 2′-*O* position of adenosine[32,33]. The methyltransferase relies on the S-adenosyl-L-methionine (SAM) to be the donor and converts SAM to the by-product, S-adenosyl-L-homocysteine (SAH). Taken together, the whole process can be sequentially depicted as GpppA-RNA → $m^7$GpppA-RNA → $m^7$GpppAm-RNA. This methylation mechanism has been partially elucidated by the structures of MTase domain with different substrates. The MTase domain is constituted mainly by a typical Rossmann fold which contains seven beta strands surrounded by four alpha helixes, two extended accessories are appended onto both N-terminus and C-terminus of the core construction[31,32]. The SAM binding site is harbored within the Rossmann fold, a central cleft beside the SAM site possesses a positively charged surface poised to interact with RNA substrate[25,34]. Interestingly, the crystal structure of DENV MTase in complex with a $m^7$GpppA-RNA substrate demonstrated the first methylation modification introduces an extra hydrophobic stacking interaction between the methyl group and a phenylalanine residue on MTase domain, providing the molecular basis of methylation sequentiality [34].

### 3.3 The domain interface regulates the enzymatic activities of NS5

Besides solely functioning their enzymatic activities, these two domains, RdRp and MTase, mutually exert impacts on each other. In the context of full-length NS5 protein, DENV MTase was shown to ensure sufficient RdRp activity by reinforcing the binding affinity of RdRp to RNA template and *de novo* dinucleotide primer, hence playing a crucial role in both initiation phase and elongation phase of RNA replication[35]. Similarly, the full-length NS5 exhibits a higher methyltransferase activity than MTase alone, whereas the addition of RdRp into MTase showed no difference on methylation level[36]. Of particular note is the physically linked MTase-RdRp being the precondition of this bilateral impact[35,36], suggesting that inner protein conformational changes are essential for the regulations. To date, crystal structures of flavivirus NS5 proteins can be categorized to two classes, with JEV NS5 and DENV2 NS5 displaying an open and extended conformation while DENV3 NS5 being more compact[37-40]. The crystallographically distinct conformations were confirmed under the solution state by small-angle X-ray scattering (SAXS)[41]. However, unlike NS5 proteins exclusively exhibiting single conformations in crystal structures, DENV3 NS5 in solution ranges from the compact form to the extended form, suggesting a highly dynamic conformation which might be involved in the mutual regulation between MTase and RdRp[41].

**4. The NS3-NS5 interaction ensures an intact viral genome producing.**

In light of RC being the primary unit of genome replication, the assembly of non-structural proteins is critical for viral life cycle. Since NS3 and NS5 are the two members with enzymatic activities among all non-structural proteins, conceivably, studying the NS3-NS5 interaction and the underlied enzymatic cooperation has become a focus in this field. Using UV cross-linking experiments, NS3 and NS5 were identified to be coupled with the 3' end of positive viral RNA strand in cell extracts[18]. The direct interaction between NS3 and NS5 was further characterized by both *in vitro* and *in vivo* methods and was shown to be essential for RNA replication[42-45]. Biochemical studies agree with the importance of this association, namely, NS5 is able to stimulate the activities of NS3 helicase and triphosphatase while the MTase guanylyltransferase is enhanced in the presence of NS3[29,46,47]. Certain residues or regions have been mapped for the NS3-NS5 interaction: residues 320-368 of NS5 engaged in the binding where Lysine 330 is the centered site, while NS3 Asparagine 570 is indispensable for its interaction with NS5 owing to mutation of asparagine to alanine interfering viral infection and viral protein production[48,49]. Even though part of the molecular basis of NS3-NS5 interaction has been addressed as mentioned above, it is still poorly understood how these enzymes systematically coordinate with each other and what kind of allosteric regulations may occur to accommodate this dynamic process of RNA replication. High-resolution

structures of NS3-NS5-RNA complex are needed to comprehensively illustrate the mechanism of running this biological machine.

## 5. An arm-race between host immune system and flavivirus

### 5.1 Innate immunity vs adaptive immunity

To fight against pathogen invasion, mammalian host has evolved a complicated immune system which can be classically categorized into two parts, innate immunity and adaptive immunity. Innate immunity evokes a rapid but nonspecific response supported by physical barriers such as skin, chemicals in blood and immune cells, performing the first line of recognizing and antagonizing foreign antigens. In contrast, adaptive immunity refers to an antigen-specific immune response, that is, once the antigen is recognized, a series of immune cells are generated by cell divisions and maturations to specifically attack the antigen. In addition, an immunological memory is formed, which permits a more efficient response to similar attack in the future.

### 5.2 Overview of innate immune response

For triggering the rapid innate immune response, a sensing system of foreign pathogens is necessary. Based upon the difference of subcellular localization, the sensing systems can be categorized into two classes. The membrane bound Toll-like receptors (TLRs) are the first class which is responsible for recognizing extracellular pathogens and viral

nucleic acids in endosomal compartment[50,51]. As for the second class, several families were shown to specifically detect intracellular pathogen-associated molecular patterns, the RIG-I like receptors (RLR), including retinoic acid-inducible gene I (RIG-I), laboratory of genetics and physiology 2 (LGP2) and melanoma differentiation associated gene 5 (MDA5), are able to recognizes cytoplasmic viral RNA, while cGAS (cyclic GMP-AMP synthase), IFI16 (interferon gamma-inducible protein 16) and other proteins perform as cytosolic sensors as well[52-55]. A classical signaling pathway cascade of sensing flavivirus infection and activating innate immune response has been revealed. The flaviviral RNA is primarily detected by RIG-I and MDA5, with RIG-I serving as a rapid sensor in early stage and MDA5 playing its role in later stage[56-59]. The sensing of viral RNA by RLR activates the inhibitors of kappa-B kinase epsilon (IKKε) and TANK binding kinase 1 (TBK-1), followed by the phosphorylation of nuclear factor kappa B (NF-κB) and interferon regulatory factor 3 (IRF3)[60]. As transcription factors, phosphorylated NF-κB and IRF3 translocate into nucleus and transcribe the genes for type I interferon (IFN) producing[52,56]. In addition ,previous studies revealed that cGAS is involved in recoginizing DENV infection by activating ER-resident factor STING to promote the generation of type I IFN[61,62]. Type I IFN is a group of cytokines which are able to invoke an antiviral state in cells and potentiate adaptive immune responses. Secreted type I IFNs are received by a heterodimeric transmembrane receptor formed by

IFNAR1 and IFNAR2, leading to the activation of Janus kinase 1 (JAK1) and tyrosine kianse 2 (Tyk2)[63]. The activated kinase proteins in turn phosphorylate IFNARs to provide docking sites for signal transducer and activator of transcription 2 (STAT2), STAT2 is then phosphorylated and recruits STAT1 to form a heterodimer[63,64]. The heterodimerized STAT1/STAT2 bind to the third component, IFN-regulatory factor 9 (IRF9), to form a trimeric complex termed IFN-stimulated gene factor 3 (ISGF3)[65]. Upon the phosphorylation of STAT1 and STAT2, ISGF3 complex translocates into nucleus and binds to IFN-stimulated response elements (ISRE) to promote the expression of hundreds of IFN-stimulated genes (ISG) for antagonizing viral infection[65]. To date, the canonical type I IFN signaling pathway has been elucidated like mentioned above, however, accumulated studies suggest the regulation of type I IFN is highly divergent, especially the assembly of ISGF3. Given a rapid reaction to non-self pathogenic particles being essentially important for innate immunity, it is conceivable that host cells have to switch themselves from resting-state to active-state within a short time. This inference is supported by the identification of basal expression of ISG, that is, host cells permanently produce a small amount of ISG which is independent of type I IFN inducing[66-68]. A preformed STAT2-IRF9 was shown to regulate the basal expression of ISG, and IFN treatment will trigger a fast switch from STAT2-IRF9 to the canonical ISGF3 complex[68]. Furthermore, under homeostatic conditions, the three components of ISGF3 exhibit

multiple combinations, including unphosphorylated STAT1 - unphosphorylated STAT2 (U-STAT1/U-STAT2), U-STAT2/IRF9 or U-ISGF3 (U-STAT1/U-STAT2/IRF9)[69]. All these combinations are suggested to serve as precursors of the canonical ISGF3, or even they are ISGF3 themselves[69]. Despite lacking a profound understanding of ISGF3 assembly, biochemical studies are partially in line with the notion that the formation of ISGF3 does not rely on a single pathway. Monomeric STAT2 has to associate with its partners to enter the nucleus, wherein the activation of a conditional NLS in STAT2 requires the phosphorylation of dimerized STAT1-STAT2, or STAT2-IRF9 complex enables STAT2 to be nuclear owing to a bipartite basic NSL in IRF9[70-73]. In light of nucleus shuttling being a crucial step for ISGF3 transcribing genes, the identification of multiple NLS regions implies potentially diverse modes of formation and activation of ISGF3 complex.

### 5.3 Flavivirus NS5 proteins antagonize innate immune response

Mouse models indicated an intact type I IFN response ensures a robust flaviviral resistance, suggesting that type I IFN is a tough barrier to flaviviral infection[74-77]. To counteract this, flaviviruses have evolved a multitude of antagonists to establish their infections. Among the most outstanding antagonist is NS5, whose mechanisms by which interfere host immunity are diverse and species-specific. DENV NS5 was shown to target human STAT2 (hSTAT2) to promote its ubiquitin-dependent degradation, thereby

inhibiting type I IFN response[78,79]. Besides a direct hSTAT2-DENV NS5 interaction, this process additionally requires a proteolytically cleaved DENV NS5 which serves as a mature form to introduce an association to a host protein, ubiquitin protein ligase E3 component n-recognin 4 (UBR4)[78,80]. UBR4 was demonstrated to stimulate the degradation of STAT2, and the first ten amino acids of DENV NS5 were mapped to interact with UBR4, especially Thr2 and Gly3 which are conserved amongst the four serotypes of DENV[80]. ZIKV NS5 and DENV NS5 share a similar manner in suppressing type I IFN, with ZIKV NS5 likewise binding to hSTAT2 and inducing the proteosomal degradation of hSTAT2[81]. However, UBR4 is not involved in ZIKV NS5-mediated STAT2 degradation[81]. This difference leads to a proteolytically-processed N-terminus of NS5 being non-essential to ZIKV diminishing hSTAT2[81]. Intriguingly, the expression of ZIKV NS5 has no influence on the stability of hSTAT1, and the infection of ZIKV enhances type II IFN that is regulated by STAT1-STAT1 homodimer[82]. YFV NS5 was also shown to bind to hSTAT2, however, this binding has to be triggered by type I IFN treatment[83]. Upon type I IFN stimulation, an E3 ubiquitin ligase TRIM23 is activated and thereafter results in a K63-linker polyubiquitination of YFV NS5, which is critical for STAT2 binding[83]. Unlike the three above mentioned flaviviral NS5 proteins targeting human STAT2 to inhibit innate immunity, JEV NS5 shuts down type I IFN response by impeding the phosphorylation of Tyk2 and STAT1 and the nuclear shuttling of STAT1,

probably contributed by protein tyrosine phosphatases (PTP) being involved in removing phosphate group from host proteins[84]. WNV NS5 was shown to interact with prolidase (PEPD) which is responsible for IFNAR1 maturation, thereby prevents the accumulation of STAT1 and suppresses type I IFN[85,86]. Taken together, these disease-causing flaviviruses commonly use NS5 as the antagonist to suppress human type I IFN. In spite of high conservatives amongst various flaviviruses, however, NS5 proteins achieve their goals in rather divergent manners. The molecular basis underpinned type I IFN suppression will help illustrate the species difference and provide insights into vaccine development.

**6. Subcellular localization of NS5 proteins**

Currently, NS5 is known to exert its functions predominantly in cytoplasm, no matter viral genome replication or host immune antagonization. Interestingly, it is also observed that NS5 translocates from cytomplasm to nucleus and accumulates to form specific geometric shapes in nucleus. DENV NS5 was first identified to contain an nuclear localization signal (NLS) within residues 369-405 which can be recognized by importin α/β, an adjacent region (residues 320-368) was further tested to be the second NLS to interact with importin β[48,87,88]. These two regions were initially assumed to confer the ability of cytoplasmic-nuclear shuttling to NS5. However, the subcellular localization of DENV NS5 was found to be serotype-dependent, where DENV2 NS5 and DENV4 NS5

are localized in nucleus but DENV1 and DENV3 mainly reside in cytoplasm[89,90]. Driven by figuring out the serotypic difference, a C-terminal flexible region (cNLS) was found to play a determinant role in nuclear localization of DENV NS5 proteins[91]. The exact functions of NS5 in nucleus have not been well established, only previous studies recommended that nuclear DENV NS5 binds to spliceosome complexes and impedes expression of antiviral factors by altering cellular splicing[92]. Similar to DENV NS5, YFV NS5 and ZIKV NS5 were also shown to predominantly accumulate in nucleus[81,83]. Using Super-Resolution Microscopy, a recent study demonstrated that ZIKV NS5 interacts with importin α to retain spherical shell-liked nuclear bodies which are exclusive of DNA[93]. A monopartite NLS located within residues 390-393 was responsible for binding to importin α, yet the C-terminus of ZIKV NS5 corresponded to cNLS of DENV NS5 didn't impact nuclear localization[93]. Collectively, the subcellular localization of flavivirus NS5 proteins seems to be divergent among species or serotypes, the underlied molecular basis and functions still remain elucidated.

**7. Treatment of flaviviruses**

To date, no drug has been approved for the treatment of flavivirus. The ongoing studies of drug discovery mainly focus on NS5, especially RdRp domain, because NS5 is critical to viral proliferation and there is no analogue in human. A successful case that can support this concept is sofosbuvir, a nucleotide inhibitor used to treat hepatitis C virus. As

a substrate analogue, sofosbuvir has to undergo a metabolic catalysis to an active triphosphate form and subsequently incorporate nascent RNA to terminate viral genome replication[94,95]. This commercially approved medication, intriguingly, has been demonstrated to improve the survival rates of ZIKV-infected mice as well, revealing an attractive prospect of developing nucleoside inhibitors to treat flavivirus[96]. In addition to a direct termination of RNA replication, small molecule which binds to allosteric pockets of RdRp and leads to its functional disability is another option. X-ray crystallographic screening of small molecule candidates revealed that specific candidates are able to associate with a pocket of DENV RdRp closed to the active site (termed "N" pocket)[39,97]. This binding is suggested to interfere the conformational changes of RdRp from its initiation state to elongation state, while the best candidates gave reasonable values in cell culture assays[39]. Although some compounds showed outstanding performance in biochemical and cellular assays, they mostly failed in animal experiments or clinical researches. The major challenges of antiviral drug discovery are cellular permeability and toxicity, thereby taking these compounds either cannot be effectively absorbed or causes severe side effects.

Vaccine is regarded as another powerful tool for antiviral therapy. A landmark of viral vaccines is YF-17D, a live-attenuated vaccine which have historically protected over millions of people from yellow fever infection. YF-17D is derived from the wild -type

yellow fever virus being serially passaged in mouse and chicken tissues[98], whereby YF-17D is able to stimulate immune response and is not lethal. However, accumulating cases were reported that YF-17D treatment might cause severe vaccine-associated diverse events, including YF vaccine-associated viscerotropic disease and YF vaccine-associated neurotropic disease[99]. In comparison with inactivated vaccine, live-attenuated vaccine readily invokes host immune response but potentially leads to diseases owing to the remained viral activity. Therefore, a fine-tuning modification system which can precisely regulate viral activity is essentially important to live-attenuated vaccine development. Conceivably, the molecular basis of flavivirus antagonizing host immune system would provide significant information for modifying the infectious efficacy of live-attenuated vaccine.

ZIKV caused a serious epidemic in 2016 which swept across almost the whole American continent, became a remarkable threat to pregnant women owing to it potentially leading to microcephaly of newborns. While the epidemic patterns of DENV display to be endemic and seasonal, and the dengue hemorrhagic fever caused by DENV is extremely dangerous or even lethal. These two flaviviruses have become an enormous burden on public health, however, currently there are no available therapies to treat them. In this study, to understand the molecular basis of flaviviral life cycle and to provide novel insights to drug or vaccine development in the future, we first solved the crystal

structure of ZIKV NS5, revealing a conserved domain conformation amongst flaivirus NS5 proteins. Further biochemical experiment verified the purified NS5 for crystallization to be enzymatically active. A small molecule inhibitor which was ever developed for targeting DENV NS5, I29, was thereafter proved to also bind to ZIKV NS5 via computationally structural superposition and X-ray crystallography. Next, we identified a multivalent binding mode between ZIKV NS5 and its host target, hSTAT2, using both crystal structure and cryo-electron microscopy (cryo-EM) structure. Biochemical and cellular assays characterized critical residues involved in this binding. Surprisingly, structure of ZIKV NS5-hSTAT2 complex indicated that ZIKV NS5 and human IRF9 (hIRF9) share a highly resembled interface when binding to hSTAT2. Pull down and co-immunoprecipitation (co-IP) experiments showed that ZIKV NS5 competes against hIRF9 to bind to hSTAT2, hence suggesting a bypass pathway for type I IFN suppression. Furthermore, we also solved the EM structure of DENV NS5-hSTAT2, demonstrating that DENV NS5 associates with hSTAT2 in a similar manner like ZIKV NS5. Finally, we are able to rescue ZIKV strains with mutations of hSTAT2-bound residues, which providing novel insights to future live-attenuated vaccine development.

## Materials and Methods

### Expression and purification of proteins

For structural and biochemical studies, the DNA sequence encoding full-length ZIKV NS5, MTase domain (residues 1-273), RdRP domains (residues 273-903) or ZIKV NS3-Hel (residues 171–617) was amplified from the cDNA of ZIKV/Macaca mulatta/UGA/MR-766/1947 and inserted into a modified pRSFDuet-1 vector (Novagen), in which the NS5 or NS3-Hel gene was preceded by an N-terminal $His_6$ - SUMO tag and ULP1 (ubiquitin-like protease 1) cleavage site. The cloning of DENV2-NS5, full-length hSTAT2, $hSTAT2_{1-713}$ and IRF9 were in the same way as those of ZIKV proteins. For *in vitro* pull-down assays, the cDNA sequence encoding full-length hSTAT2 was cloned into the pGEX6P-1 vector (GE Healthcare). The obtained plasmids were then transformed into BL21 (DE3) RIL cell strain (Agilent Technologies) for expression. Except for ZIKV NS5, the transformed cells were first grown at 37$^{o}$C and then chilled to 16$^{o}$C when $A_{600}$ reached 0.8, followed by the addition of 0.4mM Isopropyl β- d-1-thiogalactopyranoside (IPTG) for induction. While for ZIKV NS5, the cells were induced at room temperature when $A_{600}$ was 0.8 or even higher. After another 18h of cell growth, the cells were collected and the $His_6$ -SUMO-tagged protein was purified using a Ni-NTA affinity column. ZIKV NS5 was further purified on a Butyl Sepharose column (GE Healthcare) for separation from degraded protein products, followed by removal of the $His_6$ -SUMO

tag through ULP1 cleavage and size-exclusion chromatography on a Superdex 200 16/600 column (GE Healthcare) pre-equilibrated in buffer containing 25mM Tris, pH 7.5, 300mM NaCl, 5mM DTT (dithiothreitol) and 5% glycerol. As for other proteins, the $His_6$ -SUMO tag has to be removed by ULP1-mediated cleavage, followed by a series of further purification, with Butyl Sepharose column and Superdex 200 16/600 column for ZIKV MTase, DENV2-NS5 and hSTAT21-713, Q column and Superdex 200 16/600 column for ZIKV RdRp, heparin column and Superdex 200 16/600 column for IRF9 and full-length hSTAT2 and Phenyl Sepharose column and Superdex 200 16/600 column for ZIKV NS3-Hel. For GST pull-down assays, the GST-tagged full-length hSTAT2 protein was first purified using a glutathione Sepharose Fast Flow 4 column, followed by ion exchange chromatography on a Heparin column (GE Healthcare) and size-exclusion chromatography on a Superdex 200 16/600 column (GE Healthcare) using the buffer as described above. Expression and purification of ZIKV NS5 and hSTAT2 mutants followed the same approach as that for wild-type proteins

SDS–polyacrylamide gel electrophoresis analysis indicated that the purities of these proteins were qualified for subsequent experiments. Protein solution of purified proteins were preserved at -80$^{o}$C respectively.

**Crystallization and X-ray structure determination.**

Full-length ZIKV NS5 was mixed with SAH and GTP in a 1:3:3 molar ratio for

complex formation. Initial crystallization conditions were identified through sparse-matrix screens (Hampton Research Inc.). The crystals were subsequently reproduced by hanging-drop vapor diffusion method at 4?C, from drops mixed from 1ml of ZIKV NS5 and 1ml of precipitant solution (0.7–0.9M lithium sulfate, 0.1M MES, pH 6–7). Crystals were soaked for 1min in a cryoprotectant solution, comprising of crystallization buffer and 20% glycerol, before flash frozen in liquid nitrogen. As for the NS5 RdRP – hSTAT2 complex, equimolar ZIKV RdRP and $hSTAT2_{1-713}$ were mixed to achieve a final protein concentration of ~6 mg/mL. The crystallization condition was initially identified via sparse matrix screening kits (Qiagen Inc.), and further optimized through hanging-drop vapor diffusion method by mixing 1μL of the ZIKV RdRP – $hSTAT2_{1-713}$ complex with 1μL of precipitant solution (0.2M ammonium sulfate, 11% PEG 8000 and 0.1M Tris-HCl, pH 8.5). Crystals were equilibrated in a cryoprotectant comprised of precipitant solution supplemented with additional 30% glycerol, and were subsequently flash-frozen in liquid nitrogen. The acquiring of ZIKV RdRp complexed with I29 was exactly the same as that of ZIKV RdRP – $hSTAT2_{1-713}$ complex, except for an additional I29 molecule in a 1 (protein) :3 (inhibitor) molar ratio

The X-ray diffraction data for ZIKV NS5 were collected on the BL 5.0.3 beamline at the Advanced Light Source, Lawrence Berkeley National Laboratory while The X-ray diffraction data for NS5 RdRP – hSTAT2 complex and ZIKV RdRp - I29 complex were

collected on the BL 5.0.1 instead. The diffraction data were indexed, integrated and scaled using the HKL2000 program[100]. The structures were solved using the molecular replacement method in PHASER[101], with the structure of Japanese encephalitis virus NS5 (PDB ID: 4K6M) as search model for ZIKV NS5, the structure of human STAT1 (PDB ID: 1YVL) as search model for ZIKV RdRp - hSTAT2 complex. The structures were further refined by iterative model building and refinement with Coot[102] and Phenix[103], respectively. The statistics of data collection and structure determination were summarized in Table 1.

**De novo RdRp assay**

For ZIKV, the de novo RdRp reaction (20ml) contained 50mM Tris (pH 8.0), 10mM NaCl, 5mM $MgCl_2$ , 2mM $MnCl_2$ , 10mM DTT, 0.5mM ATP, 0.5mM UTP, 0.5mM GTP, 5mM CTP, 15mCi of [$\alpha$- 32 P] (10$\mu$Ci $\mu L^{-1}$ , 3,000Ci $mmol^{-1}$ ; Perkin-Elmer), 1mg of RNA template and 2mg of ZIKV NS5 protein or ZIKV NS3-Hel. The RNA template was in vitro transcribed from a PCR product using T7 polymerase (New England BioLabs). The PCR product contained a T7 promoter, followed by a cDNA fragment representing a ZIKV subgenome with deletion of nucleotides 171–10343 (GenBank accession no. KU963573.2). The de novo RdRp reaction mixtures were incubated at 23 $^{o}$C for 30min, or 33 $^{o}$C for 30, 60 and 120min. The final reactions were further extracted with phenol–chloroform and precipitated with isopropanol. The RNA pellet was dissolved in

20ml of 1x denaturing gel loading dye, and loaded onto a 10% denaturing polyacrylamide gel with 7M urea. 32 P-labelled RNA results were detected via the autoradiograph of the PAGE gel.

**Cryo-EM data acquisition**

The protein samples of $hSTAT2_{1-713}$ and ZIKV NS5 were mixed in a 1:1 molar ratio, followed by size-exclusion chromatography on a Superdex 200 10/300 column (GE Healthcare) pre-equilibrated with buffer containing 25 mM Tris-HCl, pH 7.5, 175 mM NaCl, 5 mM DTT. The peak was collected and subjected to negative stain electron microscopyfor sample optimization.

For cryo-EM sample preparation, an aliquot of 2.5 μL of the above optimized ZIKV NS5 – $hSTAT2_{1-713}$ sample at a concentration of approximately 0.5 mg/ml was applied to a Quantifoil holey carbon grid (1.2/1.3, 300 mesh), that was glow discharged for 25 seconds with a PELCO Easy Glow system. The grid was blotted and plunge-frozen in liquid ethane with a Vitrobot IV (Thermo-Fisher) at 4℃ under 100% humidity. The frozen grids were stored in liquid nitrogen before use.

For cryo-EM image acquisition, the cryo-EM grids were loaded into an FEI Titan Krios electron microscope operated at 300 kV, equipped with Gatan Quantum imaging filter (GIF) and a post-GIF K2 Summit direct electron detector. Movies were recorded as dose-fractionated frames in super-resolution mode with Legion3.1[104] at nominal

magnification of 130,000×, corresponding to a calibrated pixel size 0.535 Å on the specimen. The slit width in the GIF system was set to 20eV to remove inelastically scattered electrons. A total of 1859 movies were recorded for the data set, the dose rate on the camera was set to 1.7 electrons/pixel/s, corresponding to 6.0 electrons/Å$^2$/s. An exposure time of 8 sec was used at a rate of 0.2 s/frame, giving rise to 40 frames and a total dosage of 48 electrons/Å$^2$ for each movie. Details of the experimental conditions are summarized in Table 2.

**Cryo-EM data processing**

All but the first and last frames in each movie were motion-corrected with a subframe 5x5 to generate two motion-corrected micrographs (with and without dose-weighting), which were both binned 2x2 to yield a pixel size of 1.07Å with MotionCor2[105]. The micrographs without dose-weighting were used for contrast transfer function (CTF) determination with ctffind4.1.18[106] and for particle picking with Gautomatch (https://www.mrc-lmb.cam.ac.uk/kzhang/). The micrographs with dose-weighing were used for particle extraction and 3D reconstruction, as detailed below.

We selected 1762 micrographs by manual screening to discard those either with under-focus values greater than 3.0 μm, or containing crystalline ice. A total of 1,088,157 particles were extracted from these selected micrographs using RELION[107,108]. These particles were subjected to a reference-free 2D classification by requesting 200 classes.

Based on the presence of structures in the 2D class averages, we selected 868,048 particles (Supplementary Fig.2), which were subjected to a three-dimensional (3D) classification in RELION with C1 symmetry. The initial reference used for this 3D classification step was generated by cryoSPARC[109] from the same particles. The 3D classification was used to sort particles into 3 classes with 5 pixels and 3.8 º as the translation and rotation search parameters, respectively. 35% of the particles went to a class (the "good" class) with clear secondary structures features (Supplementary Fig.2). The particles in this "good" class were then subjected to another round of 3D classification by requesting 3 classes, which further yielded a class with improved structural features. The 118,760 particles in this class were subjected to 3D auto-refinement and post process, yielding a map at 4.0 Å resolution (Supplementary Fig.1). Data processing workflow is detailed in Supplementary Fig.S5.

The global resolution reported above is based on the ''gold standard'' refinement procedures and the 0.143 Fourier Shell Correlation (FSC) criterion. Local resolution evaluation (Supplementary Fig.1) was performed with Resmap[110].

**Atomic model building based on thecryo-EM map**

Atomic model building was accomplished in an iterative process involving Coot, Chimera[111] and Phenix. Briefly, the above crystal structure of ZIKV RdRP – hSTAT2 was fitted into the cryo-EM map as initial models by using the 'fit in map' routine in Chimera.

This fit revealed the extra density corresponding to MTase domain and the absence of density for ND, suggesting high flexibility of ND in solution (indeed, even in the crystal, ND is partially disordered). The cryo-EM densities for SH2 and partial LD were of insufficient quality for model building. The crystal structure of the MTase domain fits perfectly well into the cryo-EM density and was combined with our crystal structure of NS5 RdRP – hSTAT2$_{1-713}$ to create an initial atomic model for NS5 – hSTAT2$_{1-713}$. We then manually adjusted side chains and linker loops to match the cryo-EM density map. This process of real space refinement and manual adjustment steps was repeated until the peptide backbone and side chain conformations were optimized. Ramachandran and secondary structure restrains were used during the refinement. Our final atomic model consists of the full-length NS5 and residues 140-509 of hSTAT2 with good model geometry, as summarized in Table 2.

**Negative-stain data acquisition and structure determination.**

The protein samples of hSTAT2$_{1-713}$ and DENV-2 NS5 were mixed in a 1:1 molar ratio, and purified in the same manner as that for the hSTAT2$_{1-713}$ – ZIKV NS5 complex. Three µl of the complex sample was then applied to the carbon-coated grid and incubated for 1 min. After removal the excess sample solution, the grid was stained with 1% (w/v) uranyl formate.

Negative-stain EM micrographs were acquired manually and a TIETZ F415MP

16-megapixel CCD camera at 68,027× magnification in an FEI Tecnai F20 electron microscope operated at 200 kV. The micrographs were saved by 2× binning to yield a pixel size of 4.4 Å.

For negative-stain EM data processing, 138,246 particles were extracted from 300 micrographs using RELION. These particles were subjected to a reference-free 2D classification by requesting 100 classes. Based on the 2D class averages results, we selected 116,778 particles, which were subjected to a three-dimensional (3D) classification by requesting 3 classes. The initial reference used for this 3D classification step was generated by cryoSPARC from the same particles. Based on the 3D classification results, 35,062 particles in one class were subjected to 3D auto-refinement, yielding a map at about 17.1 Å resolution (Fig. 5a,Supplementary Fig.9e,f). The crystal structures of the MTase and RdRP domains of DENV-2 NS5 (PDB 5ZQK) and hSTAT2 (this study) were respectively fitted into the EM map by using the 'fit in map' routine in Chimera.

**GST pull-down assays**

Sixty μg of GST-hSTAT2 fusion protein was incubated with 150 μg of ZIKV NS5, in the form of either full length or individual domains, wild type or mutated, in a 1 mL pull-down buffer (10 mM Tris-Cl, pH 8.0, 100 mM NaCl, 5% glycerol, 5mM DTT and 0.1% Triton X-100) for 1 h at 4 °C. The mixtures were centrifuged at the speed of 15,000

rpm on an Eppendorf microcentrifuge 5424R for 15 minutes, followed by incubation of the supernatant with 20 µL glutathione sepharose 4 fast flow resins (GE Healthcare) for 15 minutes. Subsequently, the beads were separated from the supernatant through centrifugation at the speed of 500 rpm and subjected to two and four washes with the pull-down buffer for NS5 mutants and hSTAT2 mutants, respectively. The bound proteins were analyzed by SDS–PAGE followed by SYPRO Ruby protein gel stain (Bio-Rad). For IRF9 competition assay, the mixture of GST-hSTAT2 and ZIKV NS5 was further incubated with IRF9 in an IRF9:NS5 molar ratioof1:40, 1:20 or 1:10, followed by washes and SDS-PAGE analyses as described above.

**Electrophoretic mobility shift assay**

ZIKVNS5 – RNA complex formation was assayed with an *in vitro* transcribed, cap-1 yeast mRNA (YLR164W, 749 nt), by agarose gel electrophoretic mobility shift. NS5 and STAT2 stocks were first diluted to 1 µM in THE-300 buffer (34 mM Tris, 57 mM HEPES, adjusted to pH 7.5 with glacial acetic acid; 0.1 mM EDTA, 300 mM NaCl, 0.05% (v/v) TWEEN 20, 25% (v/v) glycerol, 2 mM DTT, 0.2 mg/mL BSA). The mRNA was diluted to 522 ng/µL (~2 µM) in water, heated to 65˚C for 5 minutes in a dry block, then snap-cooled in ice. Final samples (7.5 µL) contained RNA (52 ng/µL), NS5 (110 nM), and STAT2 (90 nM), in THE-150 buffer (composition as for THE-300 buffer, but with 150 mM NaCl). Samples were mixed, incubated for 15 minutes at room temperature

(~25˚C), and then directly loaded onto a 35 mL, pre-chilled (6 ˚C, > 30 minutes) 1% agarose gel cast with 34 mM Tris, 57 mM HEPES, pH 7.5, 0.1 mM EDTA, 10% (v/v) glycerol. The glycerol content of the samples was sufficient to allow loading in the absence of additional loading buffer. The gel was electrophoresed at 80 V in the casting buffer at 6 ˚C for 35 minutes, then stained with ethidium bromide and imaged with a Bio-Rad Gel Doc EZ imager. Images were analyzed with ImageJ.

**Cell lines and viruses**

293T, Vero and A549 cells were cultured in high glucose Dulbecco's modified Eagle's medium (DMEM) supplemented with 5 mM L-glutamine and 10% fetal bovine serum (FBS). Zika virus (ZIKV/Macaca mulatta/UGA/MR-766/1947: GenBank: KX601169.1) and VSV-GFP were grown in Vero cells. Virus titers were determined by plaque assay with Vero cells.

**Plasmids and transfections**

ZIKV NS5 and NS5 mutants were amplified by RT-PCR from total viral RNA and cloned into the pCAGGS vector. C-terminal HA or FLAG tags for these constructs were encoded in the reverse primer sequences. Dengue virus type 2 strain TSV01 (GenBank: AY037116.1) NS5, and NS5 mutants were amplified from a viral cDNA clone provided by Dr. Shou-wei Ding (University of California, Riverside Department of Microbiology

and Plant Pathology) and cloned into pCAGGS with a C-terminal HA tag encoded in the reverse primer. STAT1 and STAT2, and STAT2 mutants were cloned into pCAGGS by RT-PCR from RNA isolated from 293T cells, with C-terminal FLAG tags encoded in the reverse primer sequences. Transfections were done in 293T cells using polyethylenimine (PEI).

To generate recombinant MR766 ZIKV viruses, we generated a panel of mutants in DNA-ZIKV-MR766, the rescue system provided by Dr. Evans at Icahn School of Medicine at Mount Sinai, New York, which carried the different mutations in NS5 gene [112]. Subsequently, we rescued the ZIKV mutants following a procedure reported previously[112]. Briefly, we transfected 293T cells with the different rescue constructs and subsequently transferred the supernatant to incubate with Vero cells for viral amplification.

**Co-immunoprecipitation**

Using PEI, 1 x $10^6$ 293T cells were co-transfected with 0.5 μg each of pCAGGS encoding STAT1- or STAT2-FLAG and DENV or ZIKV NS5-HA, or their mutants. Cells were harvested 30 hours post-transfection (hpt) in NP-40 buffer (0.25% NP-40, 50 mM Tris (pH 7.4), 150 mM NaCl, 5 mM EDTA, 10% glycerol, and 1 mM PMSF). Transfected cells were subsequently lysed by rotating end-over-end at 4℃ for 15 minutes, followed by centrifugation at 15,000 rpm in 4℃ for 15 minutes. To evaluate the

interaction between ZIKV NS5 and the endogenous hSTAT2 proteins, 1 x $10^6$ 293T cells were transfected with 0.5 μg each of pCAGGS encoding ZIKV NS5-HA, WT or mutant. Cells were harvested 30 hpt and lysed. To minimize the variation of the level of endogenous hSTAT2 proteins in the immunoprecipitation procedure, we supplied the lysate of 2X$10^6$ 293T cells to each lysate sample transfected with ZIKV NS5-HA, WT or mutant. Immunoprecipitation was performed on the whole cell extract (WCE) by rotating end-over-end at 4℃ for 1 hour with 1 μg mAb anti-FLAG antibody (F1804, Sigma) or 1 μg mAb anti-HA antibody (Catalog #26183, Thermo-Fisher) followed by rotating end-over-end at 4℃ for 1 hour with recombinant protein G Sepharose 4B beads (Catalog #101243, Thermo-Fisher) pre-blocked with 5% bovine serum albumin (BSA). The beads were pelleted and washed 2 times with PBS, and bound protein was eluted by boiling in Laemmli buffer. Co-IPs and WCE were analyzed by SDS-PAGE followed by immunoblotting with mouse anti-GAPDH (Catalog #10087-384, VWR), anti-HA, and anti-FLAG primary antibodies followed by goat anti-mouse IgG (H+L) HRP-linked secondary antibody (Catalog #31160, Thermo-Fisher).

**hSTAT2 degradation assay**

To observe the degradation of endogenous hSTAT2 in the presence of over-expressed NS5 mutants, 5 x $10^5$ 293T cells were PEI-transfected with increasing amounts of pCAGGS encoding HA-tagged NS5 variants as indicated in the figure legend. At 48 hpt,

the cells were harvested in Laemmli buffer and analyzed by SDS-PAGE followed by immunoblotting with anti-GAPDH, anti-HA, and rabbit anti-STAT2 primary antibodies (Catalog #72604S, Cell Signaling) followed by anti-mouse or goat anti-mouse secondary IgG antibodies (H+L) HRP-linked (Catalog #31460, Thermo-Fisher).

**Confocal immunofluorescence microscopy**

293T cells grown on glass coverslips were co-transfected using PEI with 0.25 μg each of pCAGGS encoding hSTAT1- or hSTAT2-FLAG and ZIKV/DENV NS5-HA, or their mutants. About 48 hpt, cells were fixed and permeabilized with methanol for 20 minutes at -20 ℃, and then blocked with 3% BSA/0.2% Tween-20/PBS at 30 ℃ for 1 hour. The cells were incubated with mAb anti-HA and rabbit anti-FLAG primary antibodies (Catalog #14793S, Cell Signaling) for 1 hour at 30 ℃, followed by two 5-minute washes with PBS+0.2% Tween-20 (PBS-T). Alexa Fluor 555-conjugated anti-mouse and Alexa Fluor 488-conjugated anti-rabbit secondary antibodies were added to the cells for 1 hour at 30 ℃. After two additional washes with PBS, the coverslips were mounted onto slides with Vectashield(Vector Laboratories) containing DAPI. Images were captured using a Leica SP5 confocal microscope. Confocal laser scanning was performed using a Zeiss LSM 880 Meta (Carl Zeiss Microimaging, Thornwood, NY) fitted with a Plan Apochromatic X63/1.4 or X40/1.4 oil objective lens. Images were collected at 16 bits and at a resolution of 1024 by 1024 pixels. A total of 100 cells per condition were counted

and analyzed by microscopy. Image processing and analysis were carried out using Fiji/ImageJ software.

**VSV-GFP assay**

To determine the overall levels of IFN influenced by NS5 or NS5 mutants, 2.5 x $10^5$ 293T cells were transfected with pCAGGS encoding HA-tagged NS5 and NS5 $Mut^{YRDH}$. At 30 hpt, the transfected cells were primed with 2 μg poly(I:C) transfection. 18 hours later serial 1:2 dilutions of the supernatants from cultures transfected with the NS5 variants were used to treat A549 cells. 24 hours after supernatant treatment, A549 cells were infected with VSV-GFP (gift from Dr. Dusan Bogunovic) at MOI=1. Infected cells were visualized 24 hpi for GFP expression by the Nikon Eclipse te2000-U fluorescent microscope.

**Quantitative RT-PCR**

To quantitate ISG54 mRNA levels in the presence of NS5 or NS5 mutants, 5 x $10^5$ 293T cells were PEI-transfected with increasing amounts of pCAGGS encoding HA-tagged NS5 variants indicated in the figure legend. At 30 hpt, the transfected cells were treated with 1,000 U/mL universal type I interferon (PBL, 11200-1) for 18 hours. After IFN treatment, cells were harvested in PBS and split into two equal-volume samples. One sample was re-suspended in Laemmli buffer and analyzed by SDS-PAGE

followed by immunoblotting with anti-GAPDH and anti-HA antibodies. The second sample was used to isolate total RNA for qRT-PCR using Trizol (Catalog # N8080127, Fisher). 1 μg of RNA was reverse transcribed using random hexamer (Catalog # N8080127, Fisher). qRT-PCR was performed using iQ™ SYBR Green Supermix (Catalog # 1708880, BioRad). The ΔCt values were calculated using β-actin mRNA as the internal control. The ΔΔCt values were determined using control samples (non-transfected non-IFN-treated) as the reference value. Relative levels of transcripts were calculated using the formula 2(-ΔΔCt).

**Multi-cycle growth curve experiment**

To compare the replication kinetics of our mutant viruses to rWT ZIKV, we performed multi-cycle growth curve experiments, in which IFN-competent A549 cells or IFN-deficient Vero cellswere infected (MOI of 1) for 1 hr. with either the rescued mutant virus or the rescued WT virus. Supernatants were collected daily up to 4 days post infection, and then titers of the supernatants were determined by plaque assays in Vero cell.

## Results

### Crystal structure of ZIKV NS5 reveals a conserved domain conformation

The crystal structure of full-length ZIKV NS5 was solved at 3.3Å resolution, almost the entire sequence can be traced except the first five N-terminal amino acids, residues 747-748 and the last sixteen residues at C-terminus (Fig. 1a). The N-terminal MTase domain resides onto the top of the C-terminal RdRp domain, a linker region (residues 266-275) physically bridges these two domains (Fig. 1b). The MTase domain is predominantly constituted by a canonical Rossmann fold, where seven strands of β-sheet are sandwiched by two α-helixes. A SAH molecule was found in MTase domain (Fig. 1b), although this chemical was not intentionally added when crystallization. This is possibly due to ectopically expressed ZIKV NS5 stably binding to SAH in bacteria. Closed to the SAH binding site, a positively charged area is formed by the core Rossmann fold fragment, which is supposed to stabilize RNA strand for viral genome capping (Fig. 1b). The RdRp domain adopts a capped right-hand structure which is comprised of Palm, Thumb and Fingers subdomains, and a priming loop in Thumb subdomain blocks the putative RNA entrance (Fig. 1b). Two zinc ions are harbored within RdRp domain, as observed for the NS5 proteins of JEV and DENV3. The association between MTase domain and RdRp domain does not introduce extensive interdomain contacts, leading to a modest buried surface area of around 1400 Å.

Next, we compared the structure of ZIKV NS5 with its flaviviral counterparts, JEV NS5, DENV2 NS5 and DENV3 NS5. ZIKV NS5 superimposes well with JEV NS5, with an RMSD of 0.17 Å over 872 Cα atoms (Fig. 2a). In contrast, structural superposition of ZIKV NS5 and DENV NS5 gives a rather higher RMSD of 0.606 Å over 844 Cα atoms, mainly attributed to the differential orientation between MTase domain and RdRp domain (Fig. 2b). Unlike ZIKV NS5 and JEV NS5, DENV3 MTase sits on the top of RdRp domain in a more downward position, thereby resulting in a more compact conformation (Fig. 2b). The orientation of MTase - RdRp stacking of DENV2 NS5 is similar to that of ZIKV NS5 and JEV NS5, with an RMSD of 0.23 Å over 872 Cα atoms (Fig. 2c). It is worth mentioning that a slight movement of DENV3 MTase in comparison to ZIKV MTase and JEV MTase, resulting in differential orientations of RNA entrance and substrate binding site (Fig. 2.a,c). In accordance with published crystal structures of flavivirus NS5 proteins, DENV3 NS5 displays a "compact" fold whereas ZIKV NS5 and JEV NS5 exhibit an "open" fold, DENV2 NS5 is highly similar to "open" fold but seems to show an "intermediate" fold.

**I29 is a potential inhibitor targeting ZIKV NS5**

In light of the conserved conformation amongst flavivirus NS5 proteins, we further asked whether any small molecule inhibitor is able to target ZIKV NS5.

To address this, we first tested the enzymatic activity of our purified ZIKV NS5 protein

for crystallization. A ZIKV subgenomic RNA was artificially constructed which contains a T7 promoter followed by a ZIKV subgenome with deletion of nucleotides 171-10343 (GenBank accession no. KU963573.2) (Fig. 3a). Using the ZIKV subgenome to be the template and ZIKV NS3 helicase domain to be the negative control (Fig. 3b), we performed the *de novo* RdRp assay. ZIKV NS5 is observed to replicate RNA in a time-dependent manner, that is, along with the increase of incubation time, the RNA production is significantly improved (Fig. 3c). It is worth mentioning that a much shorter band is generated at 23$^{o}$C, indicating an insufficient reaction at low temperature (Fig. 3c). In contrast, no visible band was found in the reactions from NS3-Hel (Fig. 3c), whereby confirmed the positive bands are produced by a truly active RdRp assay and the purified ZIKV NS5 protein represents an enzymatically active form.

As mentioned in the introduction, a series of small molecule candidates bind to the "N" pocket in DENV NS5 to interfere the RNA replication (Fig. 4a)[39]. Detailed analysis of this inhibitor-binding site revealed that the critical residues for the inhibitor binding are also conserved in ZIKV NS5, arranged in a similar structural environment (Fig. 4b); therefore, suggesting that the same compound may also be inhibitory to the enzymatic activity of ZIKV NS5.

To verift our computational analysis, we further tried the co-crystallization of ZIKV RdRP and I29 inhibitor. As observed in the structure of DENV RdRp - I29 complex[39], I29

occludes the N pocket of ZIKV RdRp and is positioned in closed proximity to the priming loop (Fig. 5a). However, electron density of the I29-binding site is not in sufficient quality of modeling the entire molecule, raising the challenge of comprehensively characterizing the binding mode (Fig. 5b). This complex structure, albeit with relatively uncertain positioning of I29 molecule, provided preliminary evidence that I29 binds to ZIKV RdRp in a similar manner as DENV RdRp, thereby supports the inhibitory activity of I29 on ZIKV RdRp.

**Molecular basis of the ZIKV NS5 - hSTAT2 complex**

NS5 plays a crucial role in antagonizing host immune response. Elucidating the molecular basis of NS5 binding to host factor would provide detailed information for understanding the suppression of host immunity. Following the solved ZIKV NS5 structure, we next attempted to solve the structure of ZIKV NS5 - hSTAT2.

In line with previous study[81], our co-IP assay confimed the interaction between ZIKV NS5 and hSTAT2 while hSTAT1 showed no binding to ZIKV NS5 (Fig. 6a). We then examined which domain of NS5 is involved in the interaction. Pull down results suggested that MTase and RdRp both interact with hSTAT2 (Fig. 6b). The purification of recombinantly expressed full-length hSTAT2 gave a rather low yiled and readily degraded bands (data not shown), prompting us to search for an optimal construct for structure determination. Surprisingly, we found that a hSTAT2 fragment (residues 1-713)

showed higher stablity than full-length hSTAT2 (data not shown) and retained the ability of binding to ZIKV NS5 (Fig. 6c,d).

Using the fragment $hSTAT2_{1-713}$, the crystal structure of ZIKV RdRp - $hSTAT2_{1-713}$ was solved at 3.0 Å resolution. We were capable of defining ZIKV RdRp, the core fragment (CF, residues 137-681) and the pY-tail segment (residues 690-705) of hSTAT2, along with partial hSTAT2 ND (residues 25-68 and residues 76-112) (Fig. 7a,b,c). The CF of hSTAT2 adopts a classical elongated fold, similar to that of hSTAT1[113,114] and other STAT proteins[115-117], with the coiled-coil domain (CCD), DNA binding domain (DBD), linker domain (LD) and SRC homology 2 (SH2) domain sequentially packed against each other to form the integrated core fragment. Structural superimposition of hSTAT1 CF and hSTAT2 CF results in a root-mean-square deviation (RMSD) of 0.57 Å over 404 Cα atoms, which is consistant with the ~40% sequence identity between the CFs of these two proteins. The three subdomains of ZIKV RdRp, palm, fingers and thumb, form a right-hand cup fold (Fig. 7b), as previously observed in our crystal structure of apo-state ZIKV NS5.

Due to the lack of MTase in our crystal strucutre, we determined the cryo-EM structure of full-length ZIKV NS5 complexed with hSTAT2 for pursuing the comprehensive view. The complex structure gave an overall resolution at 4.0 Å (Fig. 7d,e, and Supplementary Fig. 1-3), with CCD, MTase and RdRP varying from 3.5 Å to 4.0 Å, DBD and LD

varying from 4.0 Å to 5.0 Å and SH2 domain changing from 5.0 Å to 5.5 Å (Supplementary Fig. 1c). The cryo-EM map is of sufficient quality to unambuiguiously model CCD and DBD of hSTAT2 and both the two domains of ZIKV NS5, while only partial LD of hSTAT2 can be fitted into the map (Fig. 7d,e, and Supplementary Fig. 3). Except for the MTase domain, the cryo-EM structure superimposes well with the crystal structure of ZIKV RdRp - hSTAT2 complex (Supplementary Fig. 4a), indicating there is no significant difference between the complex under solution state and that under crystallographic state. Taken together with these two structrues, the ZIKV NS5 - hSTAT2 complex exhibits a multivalent binding mode. The CCD domain predominantly contributes to the binding of hSTAT2 to ZIKV NS5, where the tip of CCD inserts into the inter-domain cleft formed by MTase and RdRp (Fig. 7b,c,d,e). On one side, the aromatic ring of hSTAT2 F175 stacks against H855 of ZIKV RdRp, and hSTAT2 R176 forms hydrogen bonds with RdRp residues, including the one with the backbone of G850, the bidentate one with the side chain of D734 (Fig. 8a,b). These interactions are reinforced by van der Waals contacts involving Q165, D168, Q169, D171, V172, I179, E195 and T202 of hSTAT2 CCD and V335-T337, L847, W848 and L852 of RdRP (Fig. 8b). On the opposite side, an α-helix from the MTase domain, including residues S20-K28, is positioned in close proximity to residues K218, T225, L299, R300, Q303, E306 and R310 of hSTAT2 (Fig. 8d,e), while the loop segment projected from the central β sheet of

MTase, containing residues G107-H110, is docked onto a concave surface walled by hSTAT2 Q200, L203, N204, D207, Q289, D291 and P292 (Fig. 8d,f). The ND of hSTAT2 also makes contact with ZIKV RdRp via a group of van der Waals and hydrogen bonding interactions, including D53, F61, R92, Q95, S98 and Q99 of hSTAT2 ND and T314, S317, V322, R327, A343 and I750 of RdRP (Fig. 8a,c). We were not able to trace hSTAT2 ND in the cryo-EM structure, suggesting this hSTAT2 ND - ZIKV RdRp binding is not stable in solution. Our crystal structure likewise indicates the flexibility of ND, albeit visible, the electron density of partial ND which is distant from RdRp-binding interface is poor (data not shown). Structural comparison of hSTAT2-bound NS5 with the free state ZIKV NS5 reveals a similar domain orientation between the MTase and RdRP domains(Supplementary Fig. 4b), with an RMSD of 2.3 Å over 778 aligned Cα atoms. The major difference is a modest shift of MTase domain toward the hSTAT2 CCD in the hSTAT2-bound state (Fig. 8b). The resemblance of the two states implies that ZIKV NS5 has evolved with a conformation well poised for interaction with hSTAT2. In addition, The NS5 MTase domain is anchored to the middle segment of hSTAT2 CCD, with the potential RNA binding surface of the MTase domain arching over the second and fourth helix of hSTAT2 CCD (Supplementary Fig. 4c,d). Indeed, in vitro electrophoretic mobility shift assay (EMSA) confirms that hSTAT2 competes against a capped RNA molecule for ZIKV NS5 binding (Supplementary Fig. 4e).

**The hSTAT2 interaction regulates the cellular localization of ZIKV NS5**

To test our structural observations, we selected key interaction-defining residues for mutagenesis, including Y25 from NS5 MTase, R327, D734 and H855 from NS5 RdRP, and F175 and R176 from hSTAT2. The effects of these mutations on the protein-protein interaction were analyzed by co-IP assays using 293T cells transfected with HA-tagged ZIKV NS5 and FLAG-tagged hSTAT2. Mutation to alanine of hSTAT2 F175 ($Mut^{F}$) or R176 ($Mut^{R}$) substantially reduced the binding of hSTAT2 to NS5 (Fig. 8g). Likewise, introduction of the D734A/H855A ($Mut^{DH}$), Y25A/D734A/H855A ($Mut^{YDH}$), R327A/D734A/H855A ($Mut^{RDH}$) or Y25A/R327A/D734A/H855A ($Mut^{YRDH}$) mutations on ZIKV NS5 remarkably reduced the NS5 – hSTAT2 interaction as well (Fig. 8h). In line with overexpressed hSTAT2, endogenous hSTAT2 demonstrated robust association with wild-type ZIKV NS5, but only weak interaction with the $Mut^{YRDH}$ mutant (Supplementart Fig. 5a). *In vitro* GST pull-down assay further verified the mutational effects, with the binding to hSTAT2 is gradually reduced along with the accumulation of ZIKV NS5 mutations (Supplementary Fig. 5b).

A previous study demonstrated that, as with other flaviviruses[118], ZIKV NS5 localizes predominantly within the nucleus in the absence of overexpressed STAT2; yet co-expression of ZIKV NS5 with hSTAT2 leads to their co-localization to the cytoplasm[81]. To elucidate potential impact of hSTAT2 - ZIKV NS5 interaction on the

subcellular localization of ZIKV NS5, we thereby performed immunofluorescence (IF) assays using 293T cells transfected with FLAG-tagged hSTAT2, HA-tagged ZIKV NS5. Consistent with the previous study[81], co-expressing of hSTAT2 and ZIKV NS5 led to complete retention of ZIKV NS5 in the cytoplasm, while transfection of ZIKV NS5 resulted in ZIKV NS5 resides within nucleus (Fig. 8i and Supplementary Fig. 6). In contrast, ZIKV NS5 mutants tended to translocate from cytoplasm to nucleus, especially nearly 90% of NS5 $Mut^{RDH}$ and $Mut^{YRDH}$ are localized within the nucleus (Fig. 8i and Supplementary Fig. 6). Introducing the mutations of hSTAT2-binding sites on ZIKV NS5 turned out to shape the cellular localization of ZIKV NS5, confirming the molecular basis of ZIKV NS5 - hSTAT2 interaction.

**ZIKV NS5 competes against IRF9 for hSTAT2 binding**

STAT2 and IRF9 are intrinsic partners in mammalian cells, collectively regulating type I IFN response. Previous studies demonstrated that CCD of mouse STAT2 is involved in binding to IRF9[119]. Intriguingly, the binding interface of hSTAT2 CCD - ZIKV RdRp highly resembles that of mouse STAT2 - mouse IRF9, suggesting that ZIKV NS5 and IRF9 cannot simutaneously associtate with STAT2 (Fig. 9a,b). We then designed a competitive pull-down assay to test the hypothesis. With fixed amounts of hSTAT2 and ZIKV NS5 but gradually increasing amounts of hIRF9, we observed IRF9 indeed excluded ZIKV NS5 from binding to hSTAT2, showing as opposite trends of band

intensity change of ZIKV NS5 and hIRF9 (Fig. 9c). Consistent with *in vitro* pull-down assay, *in vivo* co-IP assay utlizing 293T cells transfected with FLAG-tagged hSTAT2, HA-tagged ZIKV NS5 or Myc-tagged IRF9 indicated that increase of ZIKV NS5 reduces IRF9 precipitation and *vice versa* (Fig. 9d). In addition, F175 and R176 of hSTAT2, the two residues critical to the binding of ZIKV NS5, were also essential to interact with IRF9, with hSTAT2 $Mut^F$ or $Mut^R$ mutations leading to the disruption of hSTAT2-IRF9 complex (Fig. 9e).

**DENV and ZIKV NS5s share a similar hSTAT2-binding mechanism**

Sequence analysis of the ZIKV NS5-interaction sites of hSTAT2 shows relatively high conservation for the CCD region but less conservation for the ND (Supplementary Fig. 7a,b), which might contribute to the evolutionarily divergent interaction of STAT2 with ZIKV NS5[81]. On the other hand, the hSTAT2-interacting residues of ZIKV NS5 are considerably conserved in DENV and other members of flavivirus family (Supplementary Fig. 7c,d), raising the possibility that DENV NS5 might interact with hSTAT2 in a similar manner. To test this, we determined the EM structure of the DENV serotype 2 (DENV-2) NS5 – hSTAT2 complex (Fig. 10a and Supplementary Fig. 7e,f). Structural comparison of DENV-2 NS5 - hSTAT2 complex and free-state DENV-2 NS5 indicated a reasonable arrangement of our complex model (Fig. 10b). Indeed, DENV-2 NS5 associates with hSTAT2 in a similar manner as ZIKV NS5, with one end of the

hSTAT2 CCD embraced by both the MTase and RdRP domains of DENV-2 NS5 (Fig. 10b).

Furthermore, we mutated residues D732 and L853 of DENV-2 NS5 to alanine, equivalent to D734 and H855 of ZIKV NS5, and performed co-IP assay using 293T cells co-transfected with FLAG-tagged hSTAT2 and HA-tagged DENV-2 NS5. Wild-type DENV-2 NS5, but neither those carrying the single mutations D732A or L853A nor the double mutation D732A/L853A, interacted strongly with hSTAT2 (Fig. 4c). In addition, ectopic expression of hSTAT2 led to retention of wild-type, but not D732A/L853A-mutated DENV-2 NS5, in the cytoplasm (Fig. 4d). Together, these data suggest that DENV-2 NS5 and ZIKV NS5 engage hSTAT2 in a similar fashion.

**The ZIKV NS5 – hSTAT2 interaction leads to hSTAT2 degradation and IFN suppression**

We further evaluated the effect of the ZIKV NS5 – hSTAT2 interaction on the stability of hSTAT2 and related type I IFN response in cells. Expression of wild-type ZIKV NS5 in 293T cells led to a dose-dependent decrease on the protein level of endogenous hSTAT2 (Fig. 11a). The NS5-dependent degradation of hSTAT2 was slightly attenuated in cells transfected with NS5 $Mut^{DH}$, and became even less evident in cells transfected with NS5 $Mut^{RDH}$ or $Mut^{YRDH}$ (Fig. 11a). Next, we performed the vesicular stomatitis virus (VSV)-GFP based IFN bioassay[120] to evaluate the impact of the NS5 – hSTAT2

interaction on IFN production. The replication efficiency of VSV, which is impaired in the presence of high levels of IFN, was increased in A549 cells treated with supernatants from cell cultures transfected with wild-type NS5 compared to those treated with NS5 Mut$^{YRDH}$ (Fig. 11c), suggesting that the NS5 Mut$^{YRDH}$ mutation impaired NS5-mediated suppression of IFN production. Consistent with these results, qRT-PCR analysis of two representative type I IFN-stimulated genes, ISG54 and OAS-1, in IFN-treated 293T cells revealed that the expression of wild-type ZIKV NS5, but not NS5 Mut$^{YRDH}$, led to a dose-dependent reduction of ISG54 and OAS-1 expression (Fig. 11b). Given that previous studies have shown that ZIKV NS5, in addition to suppression of hSTAT2, inhibits interferon β production through targeting the retinoic acid-inducible gene I (RIG-I) pathway[121-123], we further interrogated the effects of ZIKV NS5 mutations on type I IFN suppression along the RIG-I signaling pathway. Toward this,we performed an IFN-β promoter-driven luciferase assay to determine whether the NS5 mutation also affects theRIG-I-(2CARD)-, TBK1-,andIRF3-activated IFN-β production. Consistent with previous observations[121-123], cells transfected with wild-type NS5, in comparison with controls, showed substantial suppression of the luciferase activity activated by RIG-I-(2CARD), TBK1,or IRF3 (Supplementary Fig. 8). Transfection with Mut$^{YRDH}$ led to a similar suppression of the luciferase activity (Supplementary Fig. 8), suggesting that this mutation did not compromise the inhibitory role of ZIKV NS5 in RIG-I pathway.

These data highlight the importance of the ZIKV NS5 – hSTAT2 interaction in proteasome-mediated degradation of hSTAT2 and downstream IFN signaling[123,124].

**The ZIKV NS5 – hSTAT2 interaction is required for efficient viral infection of IFN-competent cells**

Finally, we sought to determine the effect of the ZIKV NS5 – hSTAT2 interaction on viral infection. Toward this end, we first introduced the different NS5 mutations to the cDNA-ZIKV-MR766 construct, a rescue plasmid that has previously been used for generating recombinant MR766 ZIKV[112]. Next, we generated both the recombinant wild-type (rWT) virus and the mutant viruses through transfecting 293T cells with the cDNA-ZIKV-MR766 construct, as described previously[112]. Interestingly, the rescue plasmids carrying the Y25A ($Mut^{Y}$), H855A ($Mut^{H}$), $Mut^{RDH}$, or $Mut^{YRDH}$ failed to yield recombinant viruses, likely due to a severe attenuation effect caused by these mutations. Nevertheless, we were able to rescue viruses with wild-type or R327A NS5. Additionally, we rescued a D734A-containing virus, in which an additional mutation G338E recurrently emerged after several passages in Vero cells during two independent rescue processes. Both of these two mutant ZIKV exhibit a similar replication kinetics as rWT ZIKV in Vero cells (Fig. 12a), which is known to be deficient in IFN production[125].We then performed multi-cycle growth curve experiments using IFN-competent A549 cells, which were infected by the different mutant viruses at a multiplicity of infection (MOI)

of 1. Our results indicated that, in comparison with ZIKV rWT, both mutant viruses yielded significantly reduced virus titers after 48 hrs. post infection (Fig. 12b), suggesting an IFN-dependent attenuation effect for the R327A and G338E/D734A NS5 mutations. Together, these data establish that the hSTAT2-NS5 interaction is critical for productive ZIKV infection under IFN-competent condition.

**Disccusion**

In response to viral infection, host has developed a complicated, precise and multilayer immune system. To overcome this, virus has also evolved a series of strategies for hiding itself from host immunity or directly interfering with immune response. In this arm race, a comprehensive understanding of viral life cycle and host-pathogen interactions is important for antagonizing viral infection. NS5, the enzyme responsible for flaviviral genome replication, plays a critical role in virus proliferation and is an ideal target for drug discovery. Our crystal structure of ZIKV NS5 indicated a conserved domain conformation amongst flavivirus NS5 proteins, providing molecular basis for further drug discovery. Whilst structural superimpostions within known flavivirus NS5 structures suggested two alternative stacking orientations of MTase and RdRp, a compact fold and an open fold. This difference, albeit modest, falls in line with the notion that NS5 is dynamic and exists multiple conformations in solution[41]. Structural comparison and X-ray crystallization revealed that I29 molecule is capable of binding to ZIKV NS5, however, optimization of resolution of crystal structure , biochemical assays and cellular experiments are required for further investigation of the impact of this inhibitor on ZIKV infection. Moreover, a multivalent interaction mode between ZIKV NS5 and hSTAT2 was determined. Despite comprehensive mapping of binding sites and biochemical validation of critical residues for the NS5-hSTAT2 interaction in our study, some questions are still

remained to be addressed and new issues were raised. ZIKV NS5 was reported to bind to human STAT2 but not mouse STAT2[81], however, our structures are not able to illustrate the species difference of the binding. It is conceivable that a higher resolution structure of ZIKV NS5- hSTAT2 will provide more details on the MTase - CCD interface, which might identify human STAT2-specifc residues involved in NS5-binding. While the competitive binding to hSTAT2 of ZIKV NS5 and IRF9 suggested a bypass pathway for type I IFN suppression, or even provided a novel insight for hSTAT2 degradation. Given that hSTAT2 needs to associate with hSTAT1 or IRF9 for nuclear localization[70-73], the disruption of hSTAT2-IRF9 will lead to a significant reduction of hSTAT2 nuclear translocation. Additionally, the retention of hSTAT2 in cytoplasm likely increases the chance of being degraded, since ubiquitin-dependent proteasomal degradation occurs in cytoplasm and hSTAT2 level can be regulated naturally without viral infection. Collectively, the dissociation of hSTAT2-IRF9 by ZIKV NS5 might not only interfere with the formation of ISGF3 complex, but also play a crucial role in hSTAT2 degradation. Further cellular assays are indeed required to verify this hypothesis.

## Figures and Tables

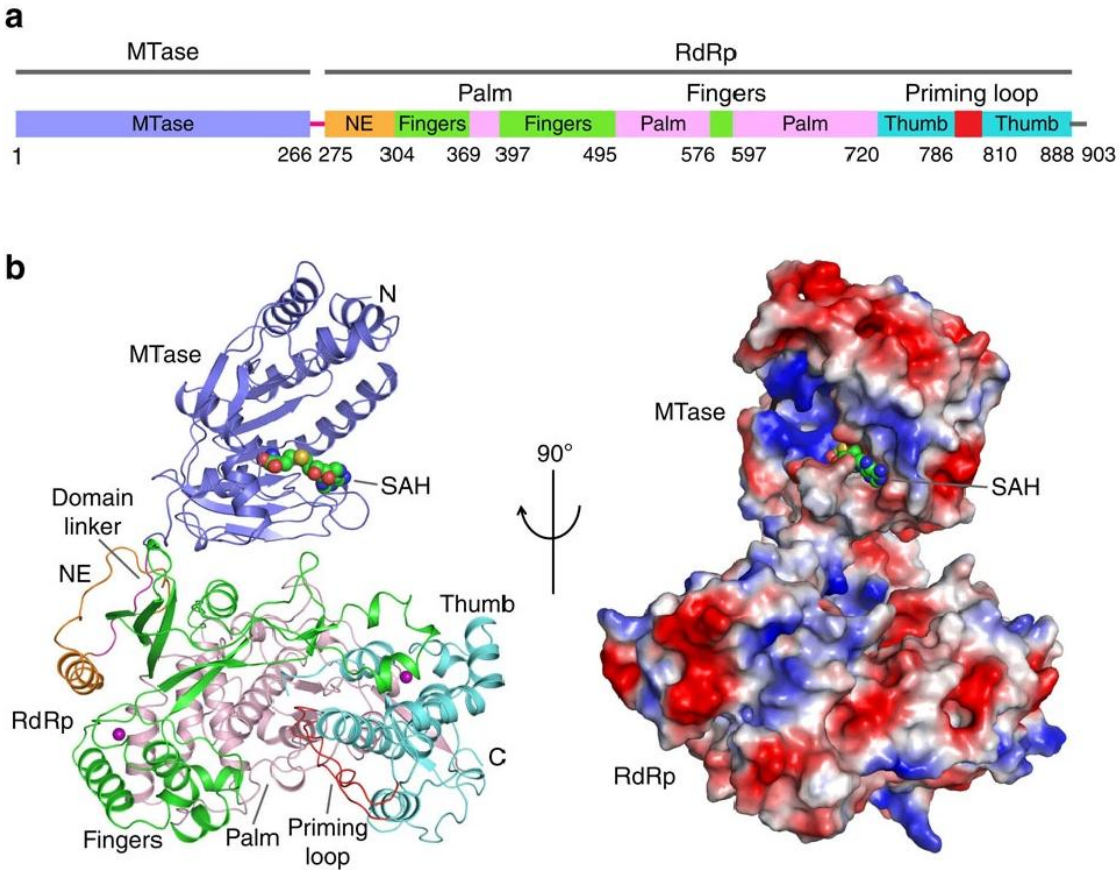


**Figure 1. Structural overview of ZIKV NS5.** (a) Colour-coded domain architecture of ZIKV NS5. (b) Orthogonal views of ribbon (left) and electrostatic surface (right) representations of ZIKV NS5. The MTase domain, the N-terminal extension, palm, fingers, priming loop and thumb of the RdRp domain, and the interdomain linker are coloured in slate, orange, pink, green, red, light blue and magenta, respectively. Zinc ions (purple) and SAH are shown in sphere representation.

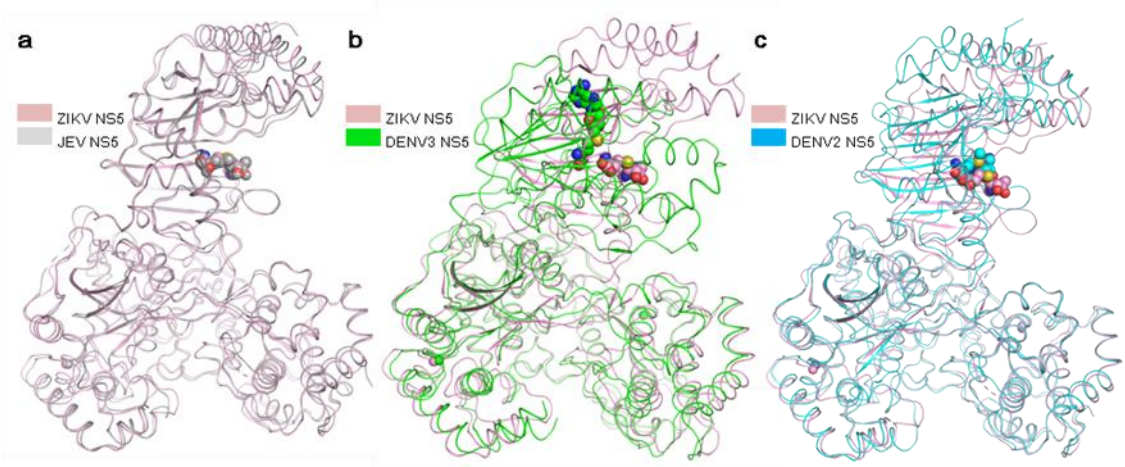


**Figure 2. Structural comparison of NS5 proteins from ZIKV, JEV, DENV3 and DENV2.** Structural comparison of ZIKV NS5 with (a) JEV NS5 (PDB ID: 4K6M), (b) DENV 3 NS5 (PDB ID: 4V0Q) and (c) DENV2 NS5 (PDB ID: 5ZQK), with ZIKV NS5 and JEV NS5 exhibiting an "open" fold, DENV3 NS5 displaying a "compact" fold and DENV2 NS5 tending to be an "intermediate" conformation but being similar to the "open" fold.

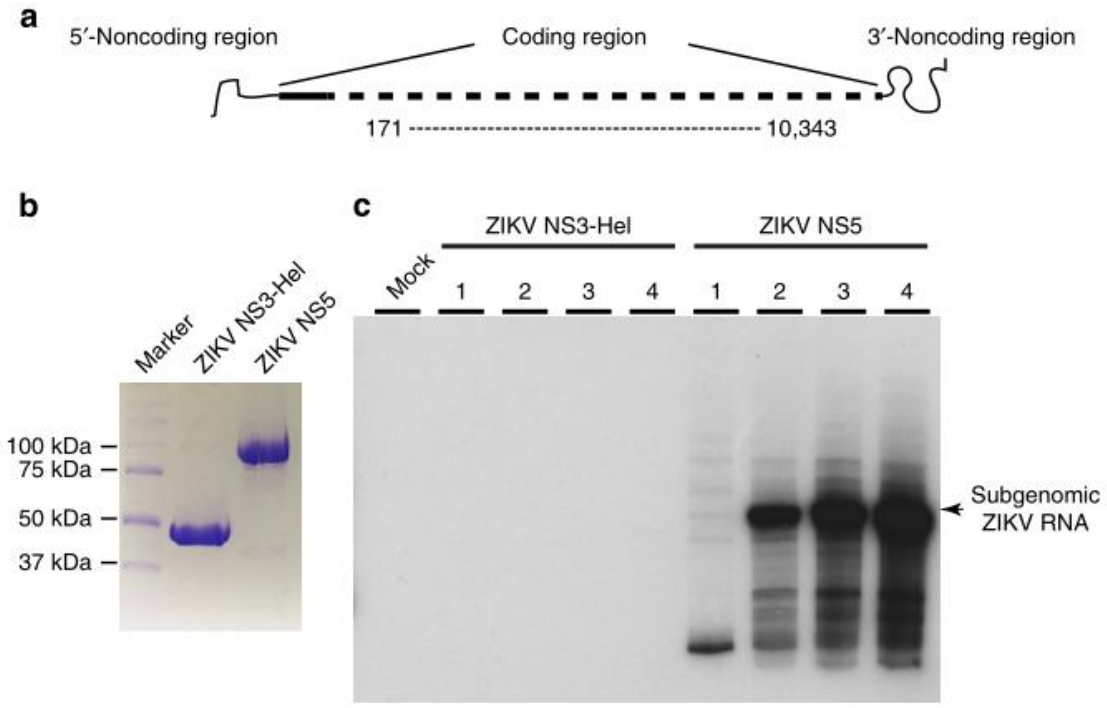


**Figure 3. De novo RNA synthesis by ZIKV NS5 protein.** (a) The subgenomic ZIKV RNA contains an internal deletion from nucleotides 171 to 10,343 (GenBank accession no. KU963573.2). (b) SDS–polyacrylamide gel electrophoresis analysis of purified ZIKV NS5 and ZIKV NS3-Hel. (c) ZIKVde novo RNA replication assay. The subgenomic ZIKV RNA was incubated with recombinant ZIKV NS5 protein, ZIKV NS3-Hel or alone (mock). The relative amount of 32 P-labelled RNA product is displayed in the autoradiograph of the PAGE gel. The reactions containing recombinant proteins were divided into four groups. Group1 was incubated at 23$^{o}$C for 30min. Groups 2, 3 and 4 were incubated at 33$^{o}$C for 30, 60 or 120min, respectively.

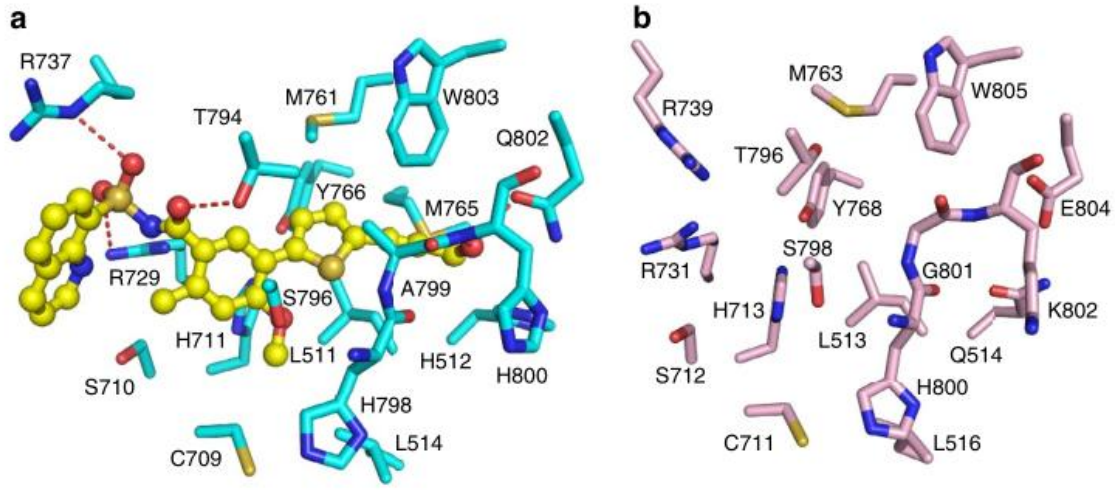


**Figure 4. Identification of a potential inhibitor-binding site in ZIKV NS5.** (a) Binding of a small-molecule inhibitor of DENV3 NS5 at its 'N pocket'. The residues of DENV3 NS5 and small-molecule inhibitor are shown in blue and yellow sticks, respectively. The hydrogen bonding interactions are depicted as dashed lines. (b) The residues of ZIKV NS5 corresponding to the inhibitor binding site of DENV3 NS5 are shown in pink sticks.

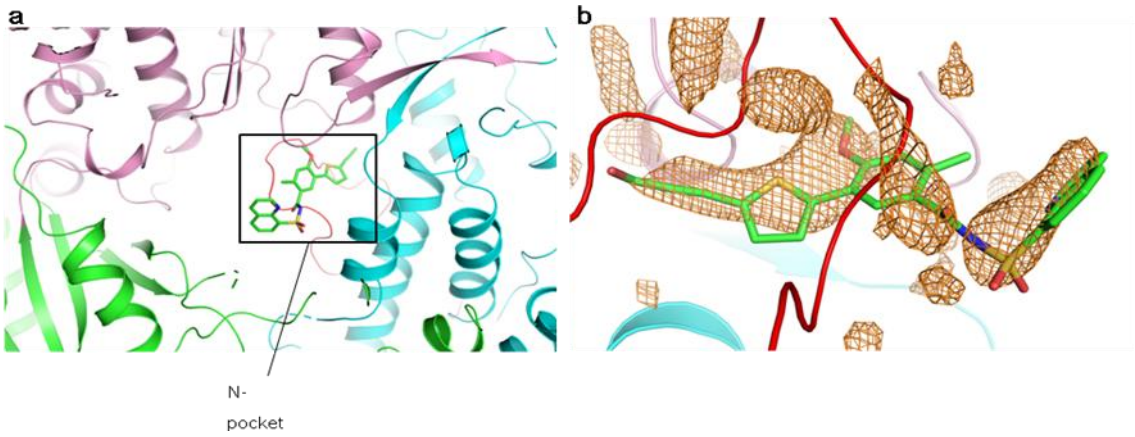


**Figure 5. Structural of ZIKV RdRp in complexed with I29 inhibitor.** (a) A close-up view of the inhibitor binding site. I29 is reprensented as sticks and colored in green. The priming loop is colored in red and the the "N" pocket is boxed. (b) $F_o$-$F_c$ map of I29 inhibitor is colored in orange and contoured at 2σ level with the carving raidus of 2 Å . As indicated in the maintext, the density is not of good quality to trace the entire molecule, especially the benzo ring in the middle.

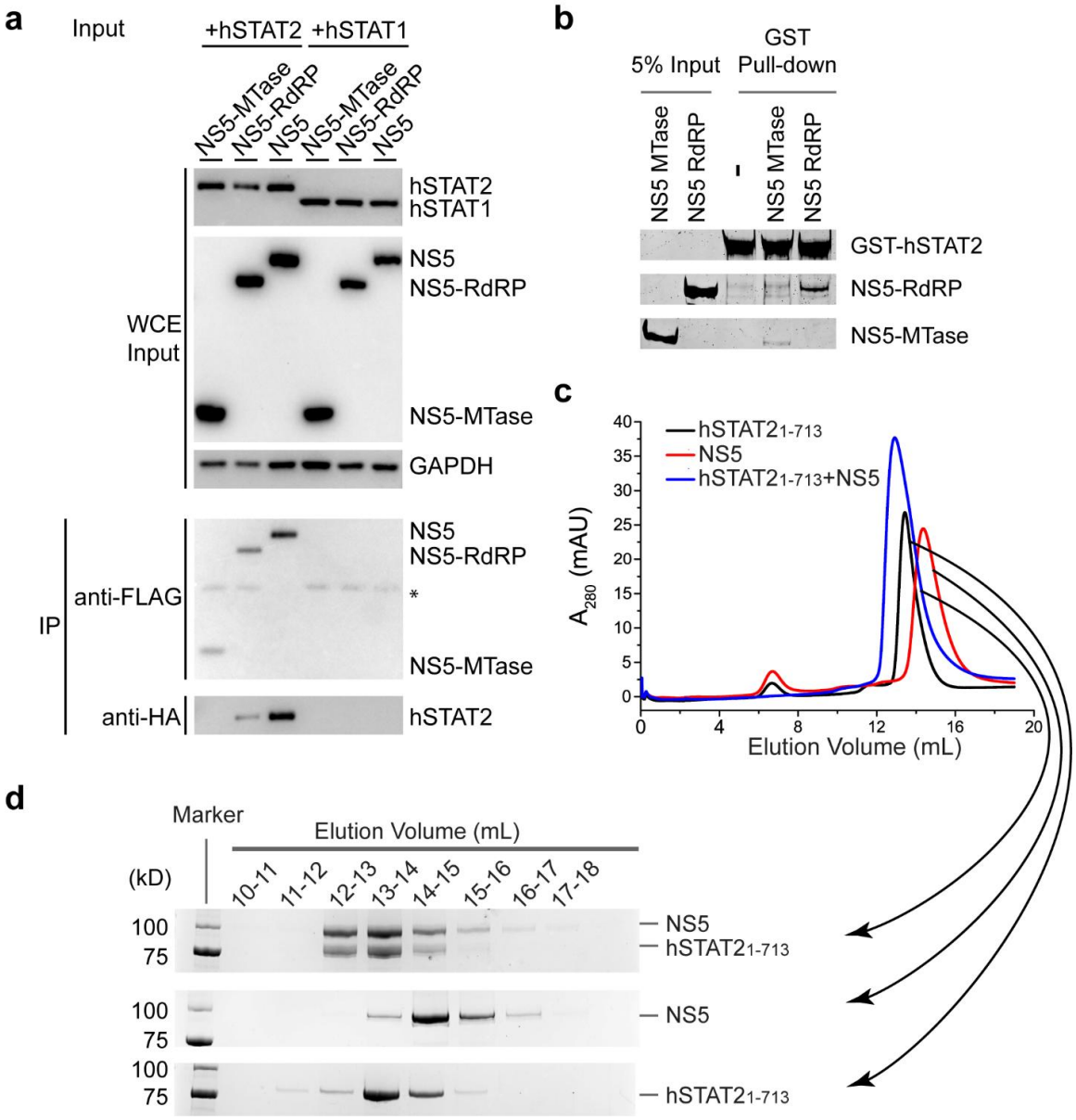


**Figure 6. Biochemical analysis of the interaction between ZIKV NS5 and hSTAT2.** (a) co-IP assay of 293T cells transfected with plasmids encoding C-terminally HA-tagged NS5 (NS5-HA) and FLAG-tagged hSTAT2 (hSTAT2-FLAG) or hSTAT1 (hSTAT1-FLAG). Immunoblot analysis of the whole cell extract (WCE) was used as input. IP was performed using antibodies against HA, FLAG and GAPDH. *antibody heavy chain. (b) GST pull-down assay of the MTase and RdRP domains of ZIKV NS5 using GST-tagged full-length hSTAT2. (c) Size-exclusion chromatography analysis of the interaction between $hSTAT2_{1-713}$ and ZIKV NS5. (d) SDS-PAGE analysis of the elution fractions in (c).

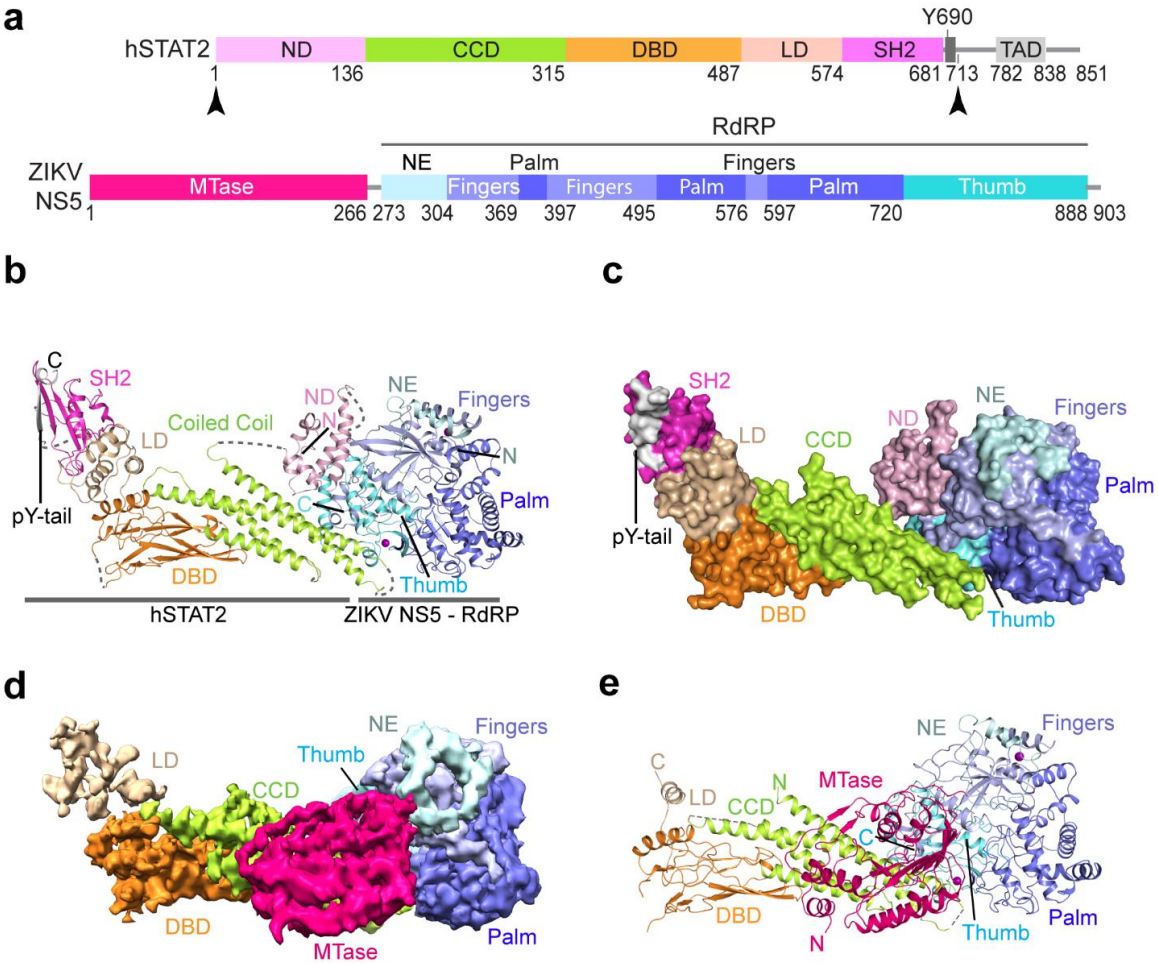


**Figure 7. Crystal and cryo-EM structures of the ZIKV NS5 – hSTAT21-713 complex**. (a) ZIKV NS5 and hSTAT2 primary sequences with domains used for crystallization marked with arrowheads. (b) Ribbon representation of the ZIKV RdRP – $hSTAT2_{1-713}$ complex. The disordered linkers are shown as dashed lines. (c) Surface representation of the ZIKV RdRP – $hSTAT2_{1-713}$ complex. (d-e) Shaded surface views of the cryo-EM density map (d) and ribbon representation of the atomic model (e) of the ZIKV NS5 – $hSTAT2_{1-713}$ complex. The color scheme in (a-e) is applied to subsequent figures unless indicated otherwise.

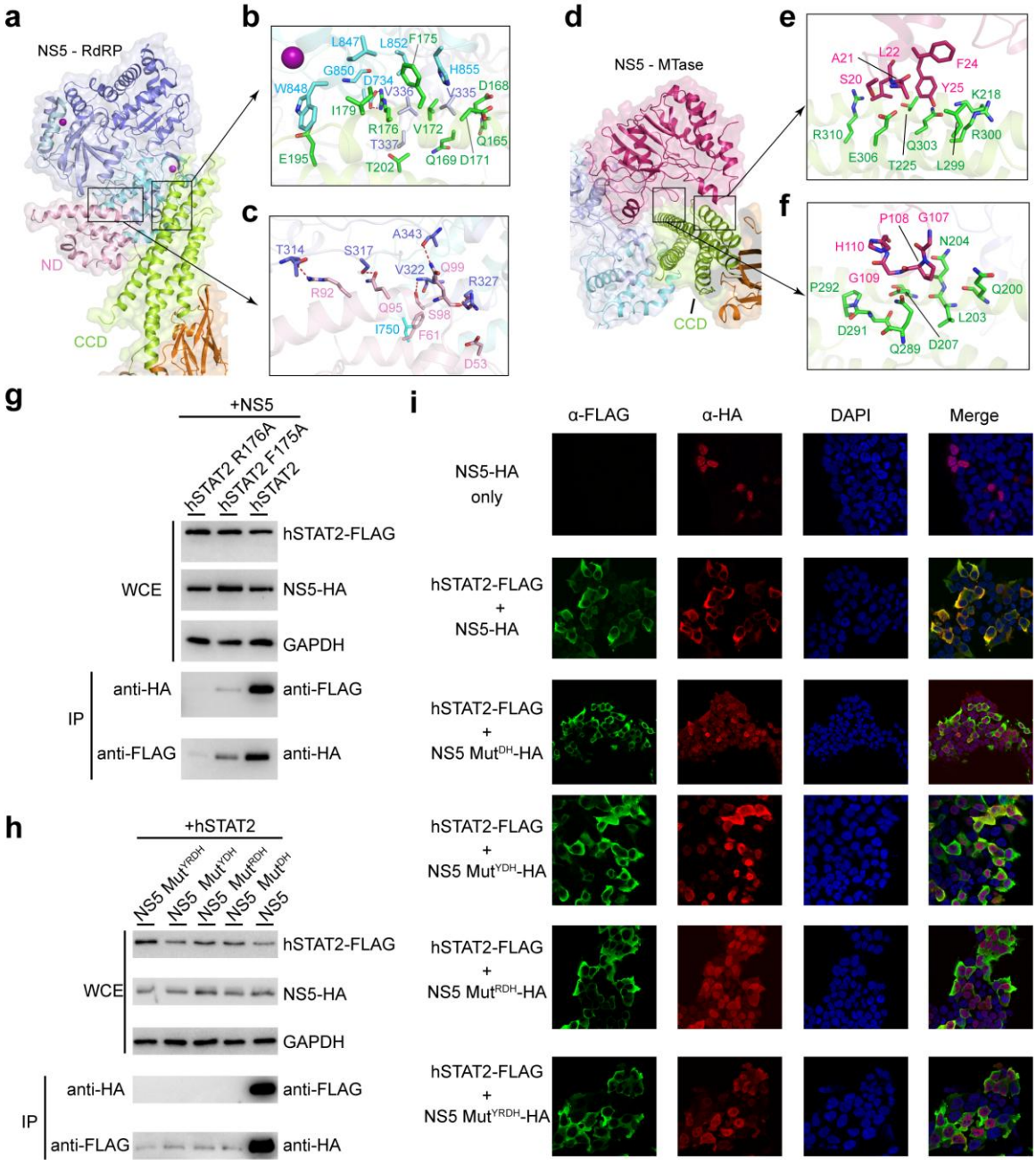
a
NS5 - RdRP
ND
CCD
b
L847
L852
F175
G850
H855
W848
D734
V336
D168
I179
V335
R176
V172
Q165
T337
E195
T202
Q169
D171
c
A343
T314
S317
V322
Q99
R327
R92
Q95
S98
I750
F61
D53
d
NS5 - MTase
CCD
e
A21
L22
F24
S20
Y25
K218
R310
Q303
R300
E306
T225
L299
f
P108
G107
H110
N204
G109
P292
Q200
L203
D291
Q289
D207
g
+NS5
hSTAT2 R176A
hSTAT2 F175A
hSTAT2
hSTAT2-FLAG
WCE
NS5-HA
GAPDH
IP
anti-HA
anti-FLAG
anti-FLAG
anti-HA
h
+hSTAT2
NS5 MutYRDH
NS5 MutYDH
NS5 MutRDH
NS5 MutDH
NS5
hSTAT2-FLAG
WCE
NS5-HA
GAPDH
IP
anti-HA
anti-FLAG
anti-FLAG
anti-HA
i
α-FLAG
α-HA
DAPI
Merge
NS5-HA only
hSTAT2-FLAG + NS5-HA
hSTAT2-FLAG + NS5 MutDH-HA
hSTAT2-FLAG + NS5 MutYDH-HA
hSTAT2-FLAG + NS5 MutRDH-HA
hSTAT2-FLAG + NS5 MutYRDH-HA

**Figure 8.Cellular analysis of the ZIKV NS5 – hSTAT2 interaction.** (a-c) Ribbon and surface view showing NS5 RdRP – hSTAT2 interaction (a), with the details for the CCD- and ND-mediated interactions further highlighted in expanded views (b)and (**c**), respectively. Hydrogen bonds in (**b**) and (c) are shown as dash lines. (d-f) Ribbon and surface view of the NS5 MTase – hSTAT2 interaction (d), with details highlighted in expanded views (e) and **(**f**)**. (g-h) Co-IP analysis showing the effects of hSTAT2 mutations (g) and NS5 mutations (h) on the NS5 – hSTAT2 interaction. Immunoblot analysis of the IP and whole cell extract (WCE) was performed using antibodies against HA, FLAG and GAPDH.(i**)** IF analysis of 293T cells transfected with plasmids encoding NS5-HA and/or hSTAT2-FLAG. The transfected cells were fixed for immune staining using antibodies against HA (Red) and FLAG (Green). Nuclei were visualized by DAPI (blue) counter staining.

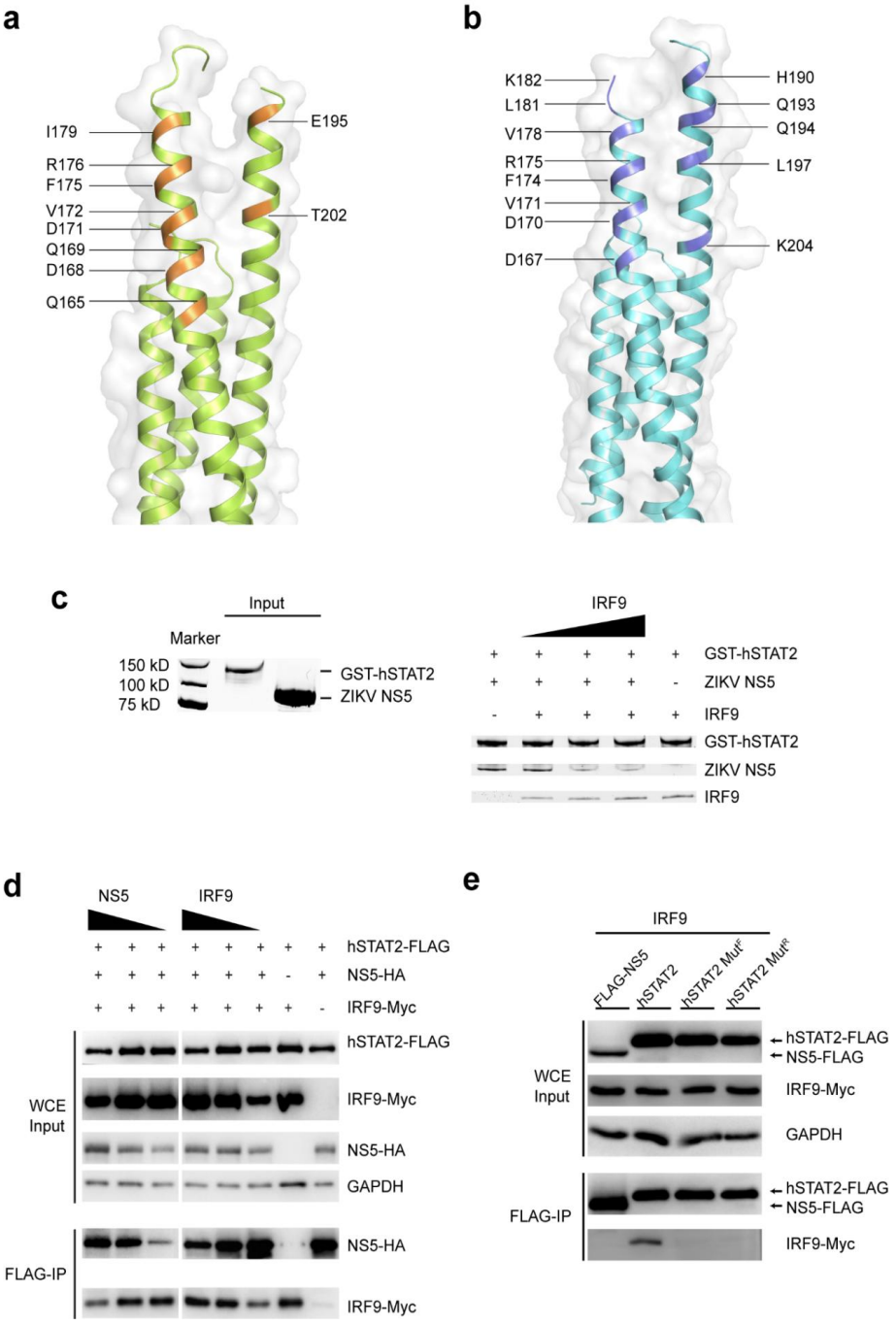


**Figure 9. ZIKV NS5 competes against IRF9 for hSTAT2 binding. (**a) Ribbon and surface view of the ZIKV NS5-binding sites (orange) of hSTAT2 CCD. (b) Ribbon and surfaceview of the ZIKV NS5-binding sites (blue) of mouse STAT2 CCD. (c) *In vitro* pull-down assay of ZIKV NS5 using GST-hSTAT2 in the presence of various amount of IRF9. (d) Co-IP assay of HA-tagged ZIKV NS5 (NS5-HA), FLAG-tagged hSTAT2 (hSTAT2-FLAG) or hSTAT1 (hSTAT1-FLAG) and Myc-tagged IRF9 (IRF9-Myc). (e) IP assay of endogenous hSTAT2 with HA-tagged ZIKV NS5 (NS5-HA), wild type.

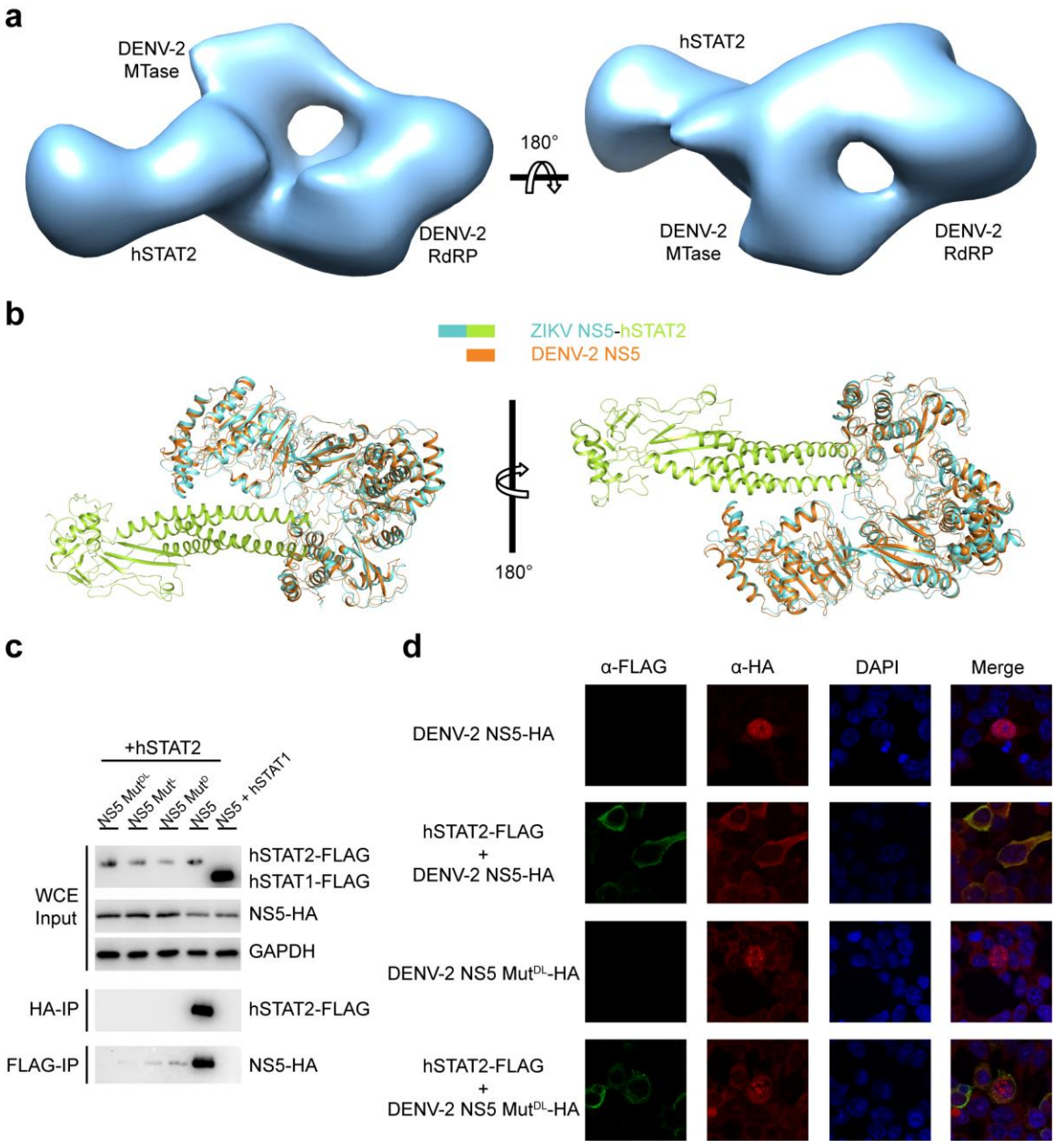
a
DENV-2
MTase
hSTAT2
DENV-2
RdRP
180°
hSTAT2
DENV-2
MTase
DENV-2
RdRP
b
ZIKV NS5-hSTAT2
DENV-2 NS5
180°
c
+hSTAT2
NS5 Mut^DL
NS5 Mut^I
NS5 Mut^P
NS5
NS5 + hSTAT1
WCE
Input
hSTAT2-FLAG
hSTAT1-FLAG
NS5-HA
GAPDH
HA-IP
hSTAT2-FLAG
FLAG-IP
NS5-HA
d
α-FLAG
α-HA
DAPI
Merge
DENV-2 NS5-HA
hSTAT2-FLAG
+
DENV-2 NS5-HA
DENV-2 NS5 Mut^DL-HA
hSTAT2-FLAG
+
DENV-2 NS5 Mut^DL-HA

**Figure 10. Analysis of the DENV NS5 – hSTAT2 interaction. (**a**)** Fitting of the crystal structures of the MTase and RdRP domains of DENV-2 (PDB 5ZQK) and $hSTAT2_{141-490}$ (this study) within EM density. **(**b**)** Superposition of the crystal structure of free DENV-3 NS5 (grey) and the cryo-EM structure of hSTAT2-bound DENV-2 NS5 (orange).For clarity, only the CCD of hSTAT2 (green) is shown in the complex structure. **(**c**)** Co-IP assay of HA-tagged DENV-2 NS5 (NS5-HA), FLAG-tagged hSTAT2 (STAT2-FLAG) or hSTAT1 (hSTAT1-FLAG). The D732A, L853A and D732A/L853A mutations are denoted as $Mut^{D}$, $Mut^{L}$ and $Mut^{DL}$, respectively. **(**a**)** IF analysis of 293T cells transfected with plasmids encoding DENV-2 NS5-HA and/or hSTAT2-FLAG. The transfected cells were fixed for immune staining using antibodies against HA (Red) and FLAG (Green). Nuclei were visualized by DAPI (blue) counter staining.

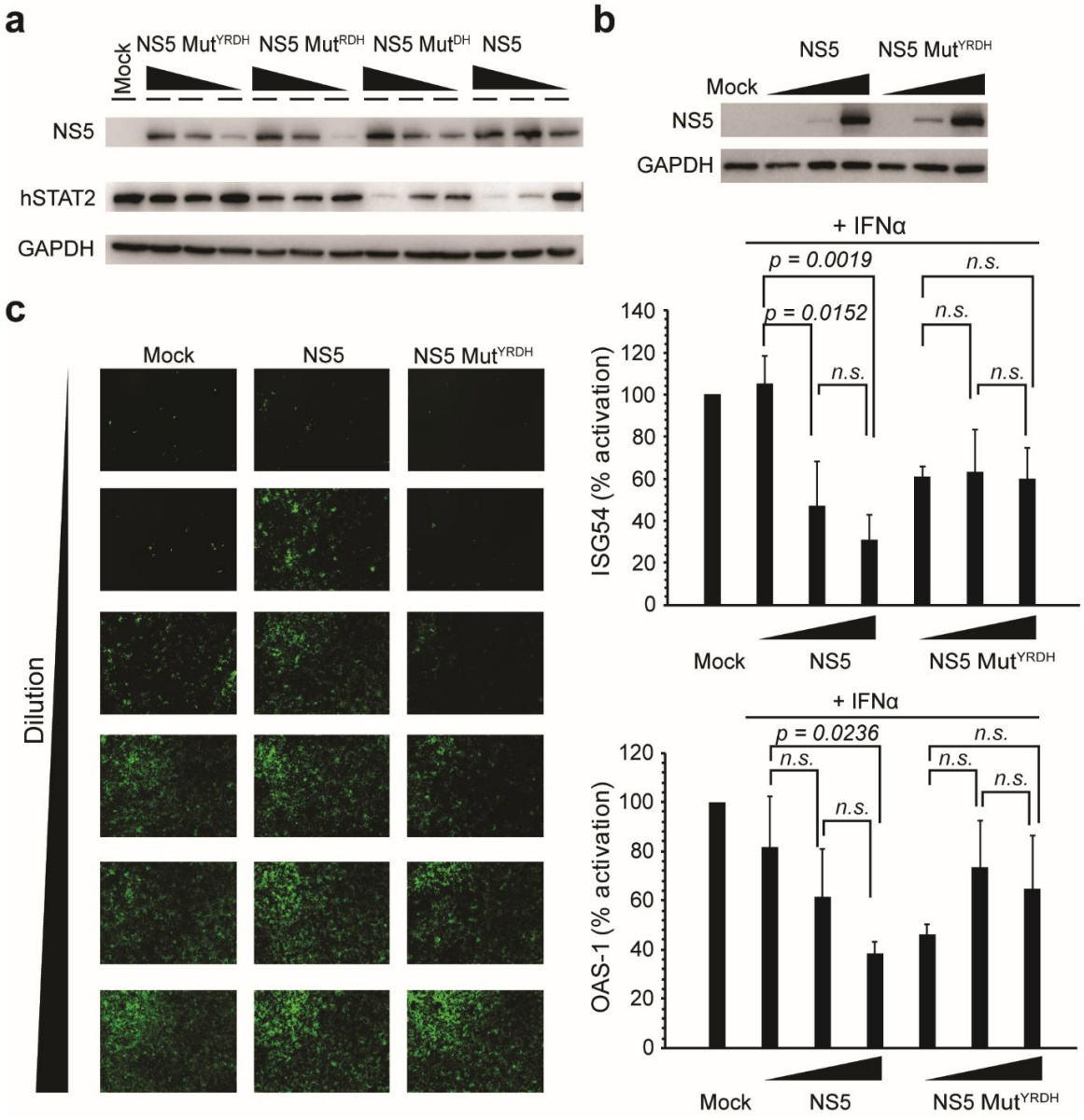


**Figure 11. Role of the ZIKV NS5 – hSTAT2 interaction in ZIKV NS5-mediated degradation of hSTAT2 and type I IFN signaling suppression. (**a**)** Immunoblot analysis of 293T cells transfected with indicated plasmids encoding wild-type or mutant NS5-HAs at three different amounts using antibodies against HA, hSTAT2, and GAPDH. **(**c**)** VSV-GFP infection of A549 cells treated with 1:2 serial dilutions of the supernatants derived from poly(I:C)-stimulated 293T cells, non-transfected (mock), or transfected with NS5 or NS5 Mut$^{YRDH}$. **(**b**)** qRT-PCR analysis of ISG54 and OAS-1 mRNAs of non-transfected 293T cells (mock), or cells transfected with plasmids encoding wide-type or mutant NS5-HAs, followed by treatment with IFN for 18 hr. Error bars represent s.d. of triplicate experiments. Statistical analysis used two-tailed Student's t-test. ns, $p > 0.05$.

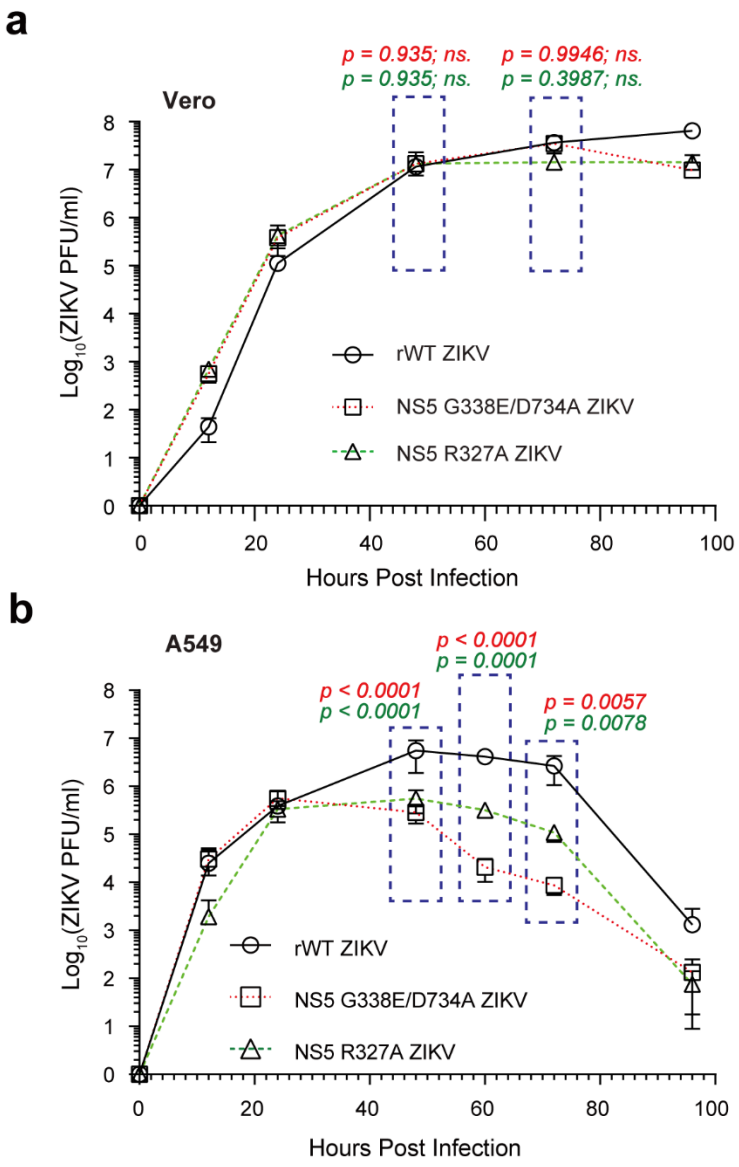


**Figure 12. Role of the ZIKV NS5 – hSTAT2 interaction in ZIKV infection. (**a-b**)** Growth curves of Vero (a) and A549 **(**b**)** cells infected with the rWT and mutant MR766 viruses. Values of titers are expressed in PFU per milliliter. Means and standard errors were estimated from 3 independent experiments, with each performed in triplicate. Statistical analysis used the two-way ANOVA test. ns, $p > 0.05$.

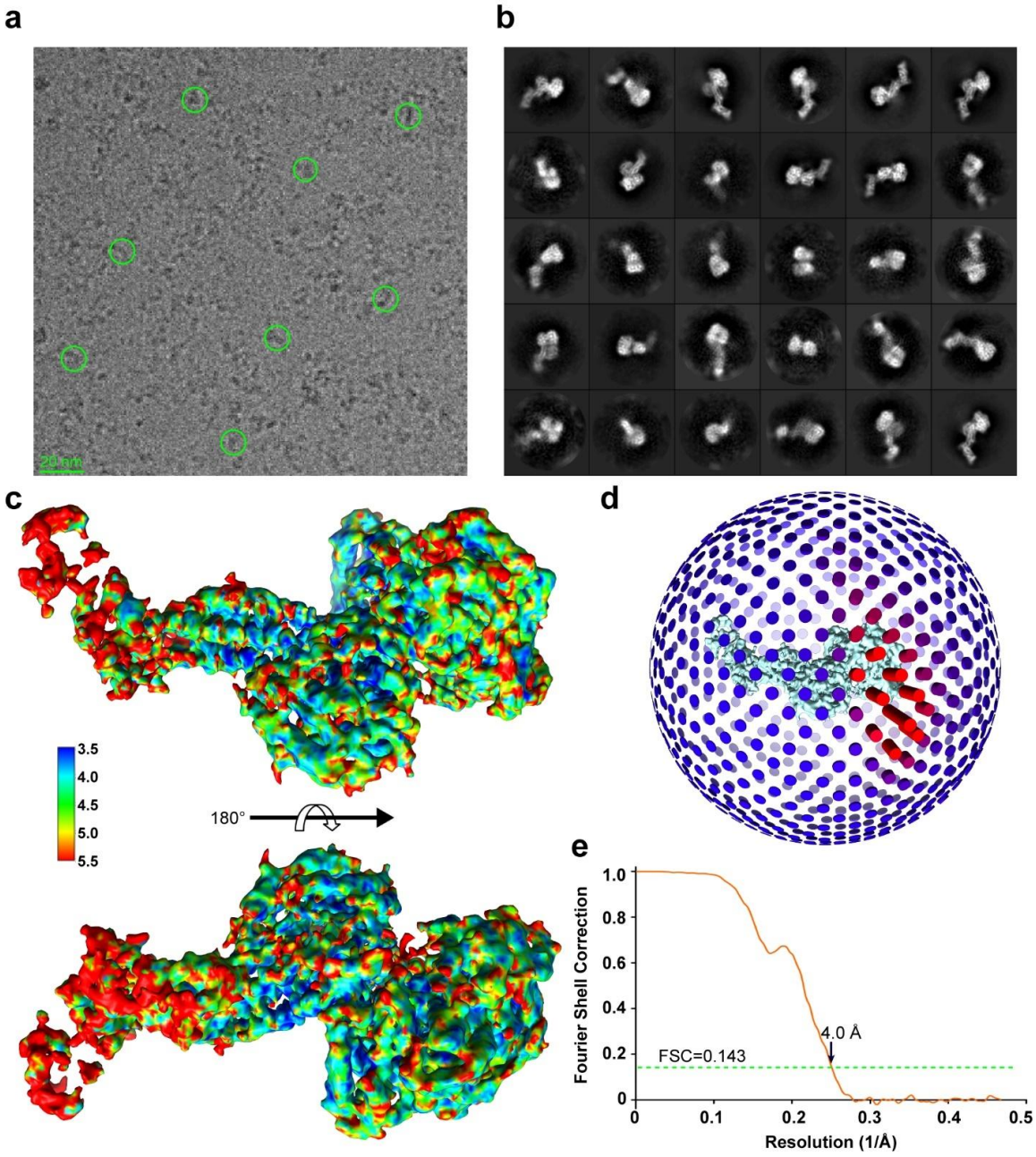


**Supplementary Figure 1. Cryo-EM analysis of the ZIKV NS5 – hSTAT2 complex. (**a**)** A representative cryo-EM micrograph with select particles circled. **(**b**)** Representative 2D class averages. **(c)** Local resolution evaluation of the reconstructed map by Resmap[110]. **(**d-e**)** Angular distribution (d) and global resolution evaluation based on "gold-standard" Fourier shell correction (FSC) (e), both generated by RELION[107,108].

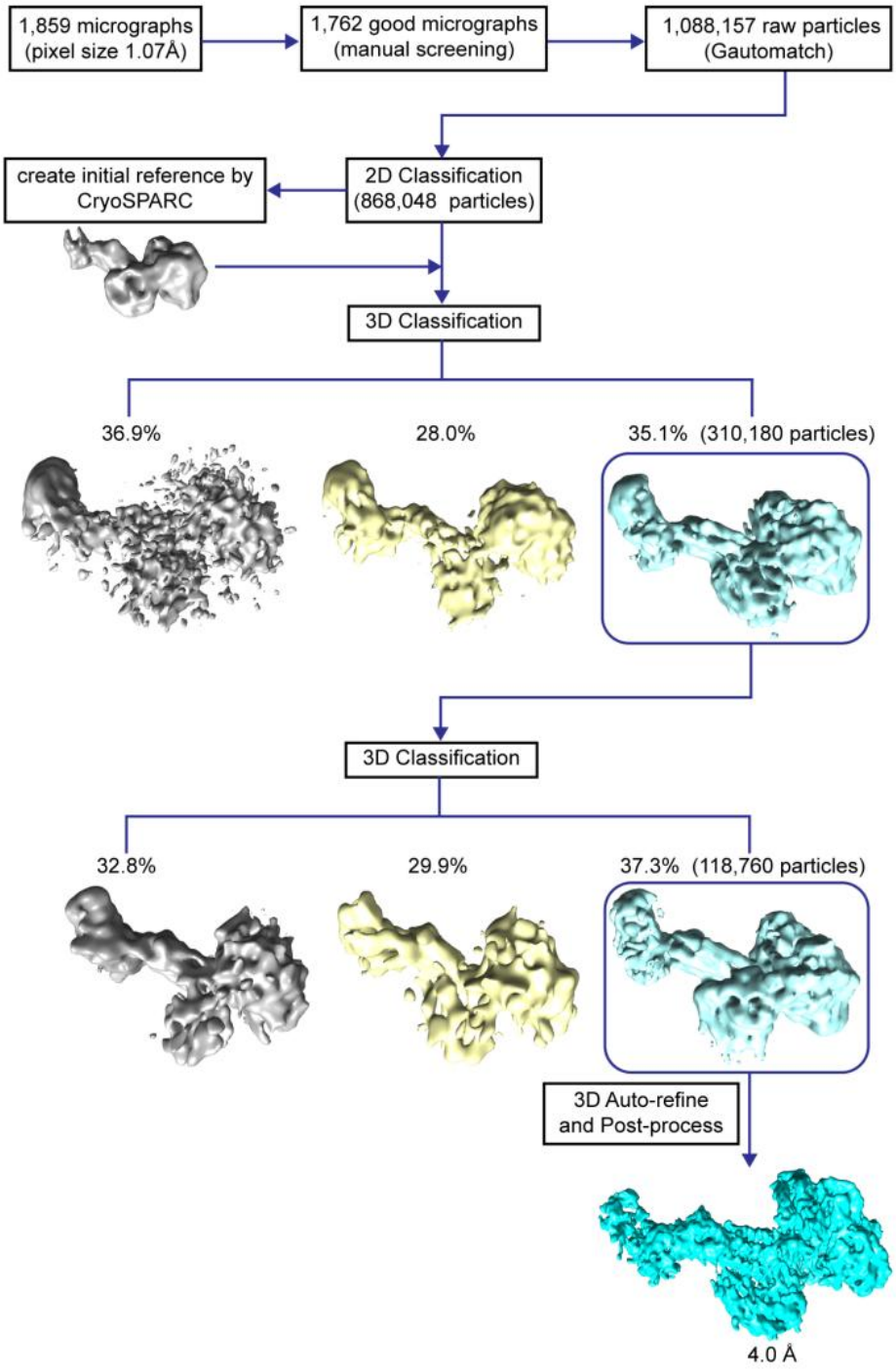


**Supplementary Figure 2. Data processing workflow used for cryo-EM reconstruction of the ZIKV NS5 - hSTAT2 complex.**

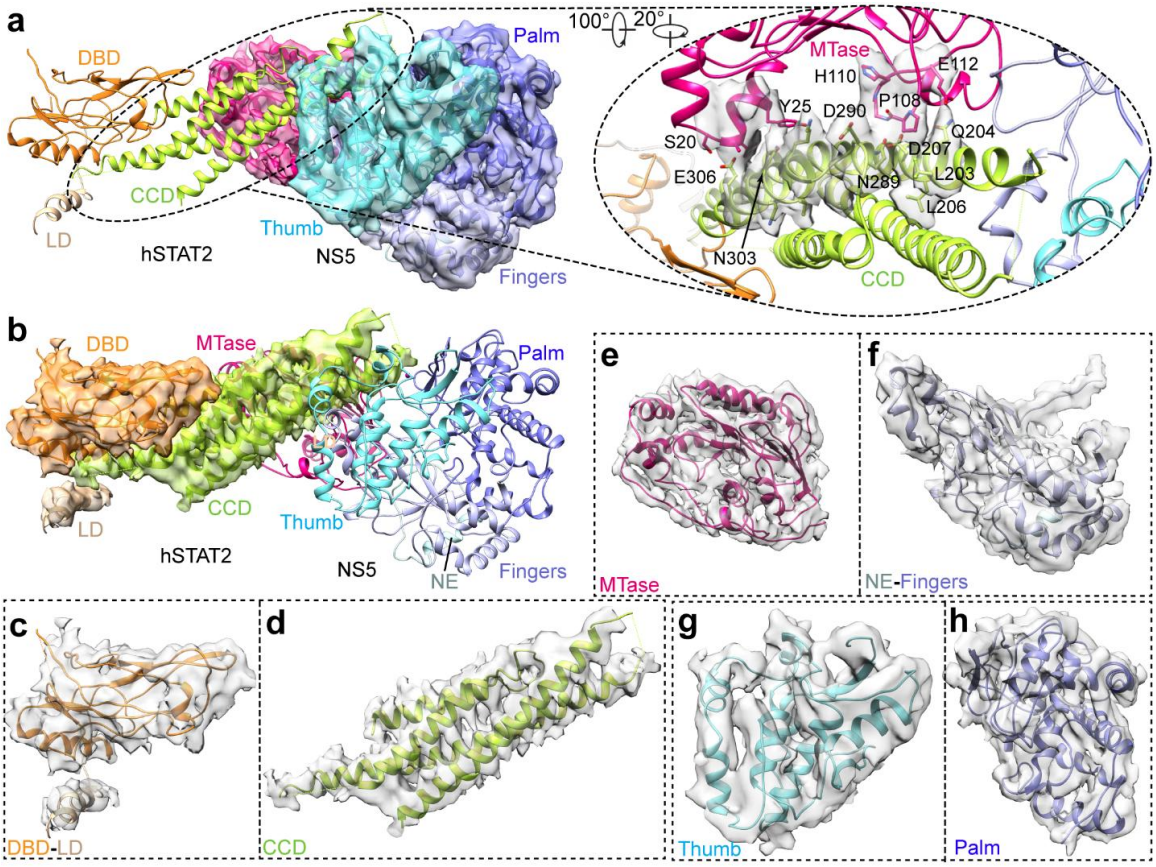


**Supplementary Figure 3. Details of the cryo-EM densities overlaid with their atomic models (ribbon) of the domains in ZIKV NS5 – hSTAT2 complex. (**a-b**)** Ribbon representations of the atomic model of NS5 – hSTAT2, with NS5 (a) and hSTAT2 (b) overlaid with their respective density maps. N- and C-termini are indicated by letter 'N' and 'C'. Two main interfaces between the MTase and CCD domains are shown in inset. **(**c-d**)** DBD, LD and CCD domains in hSTAT2. **(**e-h**)** MTase, NE, Fingers, Thumb and Palm domain in NS5.

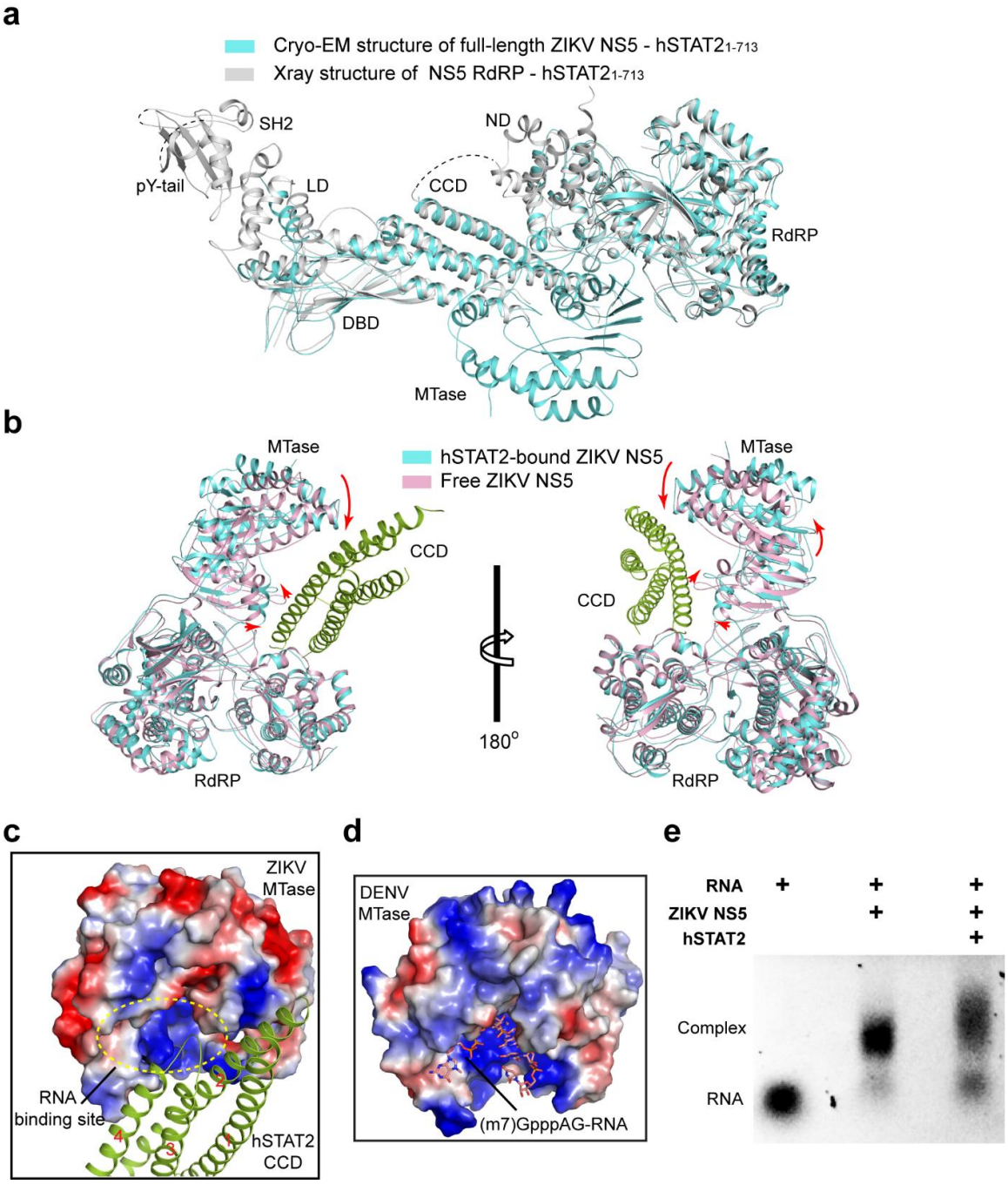
a
Cryo-EM structure of full-length ZIKV NS5 - hSTAT2 1-713
Xray structure of NS5 RdRP - hSTAT2 1-713
SH2
pY-tail
LD
ND
CCD
RdRP
DBD
MTase
b
MTase
hSTAT2-bound ZIKV NS5
Free ZIKV NS5
CCD
RdRP
180°
MTase
CCD
RdRP
c
ZIKV
MTase
RNA
binding site
hSTAT2
CCD
d
DENV
MTase
(m7)GpppAG-RNA
e
RNA
ZIKV NS5
hSTAT2
Complex
RNA

**Supplementary Figure 4. Structural analysis of the ZIKV NS5 – hSTAT2 interaction.** (a) Superposition of the crystal structure of NS5 RdRP – $hSTAT2_{1-713}$ (grey) and the cryo-EM structure of full-length NS5 – $hSTAT2_{1-713}$ (cyan). While the cryo-EM structure contains the MTase domain, there is no change in the relative orientations of different domains between the two structures. (b) Structural superposition of free (PDB 5TMH) and hSTAT2-bound ZIKV NS5. The conformational transition of the MTase domain of ZIKV NS5 from free state to the hSTAT2-bound state is indicated by arrows. For clarity, the hSTAT2 domains, other than the CCD, were removed. (c) Surface view of the MTase domain of ZIKV NS5 bound to hSTAT2 CCD (green ribbon). The four helices of the CCD are sequentially numbered from '1' to '4'. The potential RNA binding site is indicated by dashed circle. (d) Surface of the DENV-3 MTase bound to viral cap-0 RNA (PDB 5DTO). (e) hSTAT2 inhibition of ZIKV NS5 – RNA binding assayed by electrophoretic mobility shift. Addition of NS5 to a cap-1 ($m^7GpppG_{2'OMe}$) yeast mRNA (YLR164W, 749 nt) resulted in a shift of the RNA band. Further addition of STAT2 resulted in release of RNA from the NS5 – RNA complex, with concomitant accumulation of free RNA.

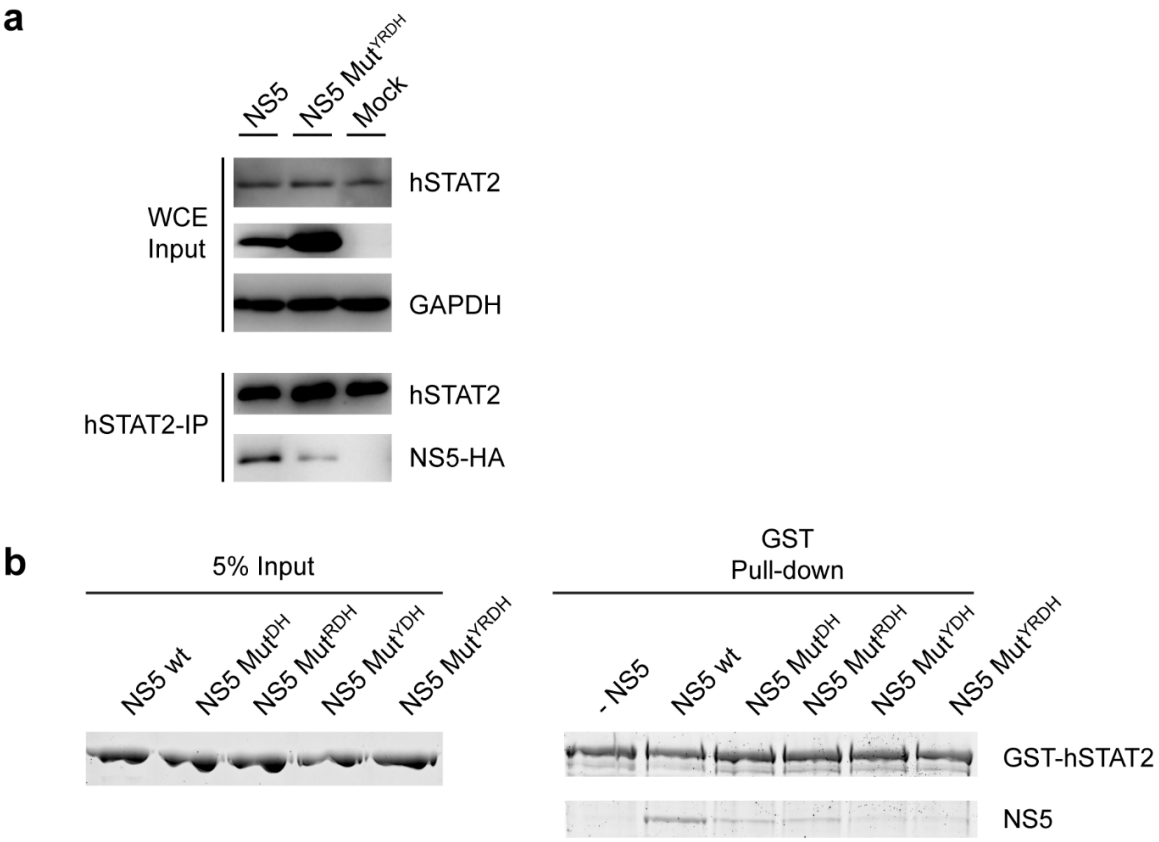


**Supplementary Figure 5. Analysis of the interaction between ZIKV NS5 and hSTAT2.** (a) IP analysis of endogenous hSTAT2 in 293T cells transfected with WT or mut$^{YRDH}$ NS5. Immunoblot was performed using antibodies against hSTAT2, HA, and GAPDH. (v) *In vitro* pull-down assay of ZIKV NS5 mutations using GST-hSTAT2 as bait. wt: wild type.

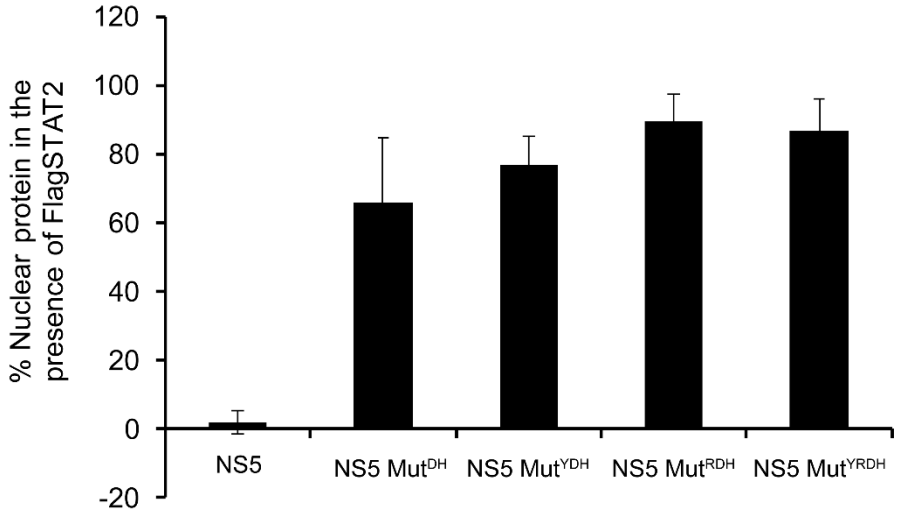


**Supplementary Figure 6. Quantification of nuclear localization of NS5, WT or mutants.**

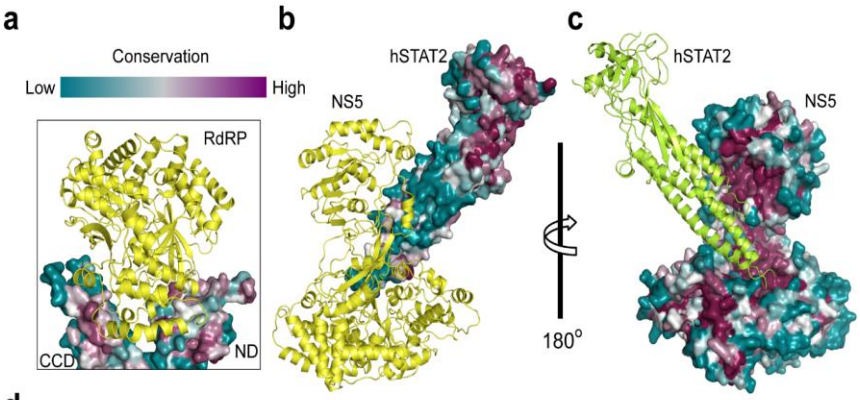


d

hSTAT2-CCD binding sites

| | | | | | | | | | |
|---|---|---|---|---|---|---|---|---|---|
| ZIKV | 18 | QMSALEFYSYKKSG | 31 | | 104 | TKGGPGHEEP | 113 |
| SPOV | 19 | RMTALEFYAYKRSG | 32 | | 105 | TKGGAGHEEP | 114 |
| WNV | 18 | QMTKEEFTRYRKEA | 31 | | 104 | TKGGPGHEEP | 113 |
| DENV-2 | 19 | ALGKSEFQIYKKSG | 32 | | 104 | TKGGPGHEEP | 113 |
| YFV | 18 | LLDKRQFELYKRTD | 31 | | 104 | TLGRDGHEKP | 113 |

hSTAT2-CCD binding sites

| | | | | | | | | | | | | |
|---|---|---|---|---|---|---|---|---|---|---|---|---|
| ZIKV | 332 | PWDVVTGVT | 340 | 733 | QDEL | 736 | 845 | EDLWCGSLIGHRP | 857 |
| SPOV | 333 | PWDALSSVT | 341 | 734 | QDEL | 737 | 846 | EDLWCGSLIGHRP | 858 |
| WNV | 333 | PWDTITNVT | 341 | 736 | QDEL | 739 | 848 | EDIWCGSLIGTRA | 860 |
| DENV-2 | 331 | PWDIIPMVT | 339 | 731 | QDEL | 734 | 843 | EDQWCGSLIGLTS | 855 |
| YFV | 332 | PWDRIEEVT | 340 | 735 | QDEL | 738 | 847 | QDKLCGSLIGMTN | 859 |

hSTAT2-ND binding sites

| | | | | | | | | | | | | |
|---|---|---|---|---|---|---|---|---|---|---|---|---|
| ZIKV | 312 | APTQGSASSLVNGVVRLL | 329 | 341 | GIAMT | 345 | 748 | WSIRE | 752 |
| SPOV | 313 | ADTQGSASSMVNGVVRLL | 330 | 342 | NIAMT | 346 | 749 | WSLSE | 753 |
| WNV | 313 | VKPTGSASSLVNGVVRLL | 330 | 342 | TMAMT | 346 | 751 | WNVRD | 755 |
| DENV-2 | 311 | TKQTGSASSMINGVVKLL | 328 | 340 | QNAMT | 344 | 746 | WSLRE | 750 |
| YFV | 312 | TKTSGSAASMVNGVIKIL | 329 | 341 | RMAMT | 345 | 750 | WMIKE | 754 |

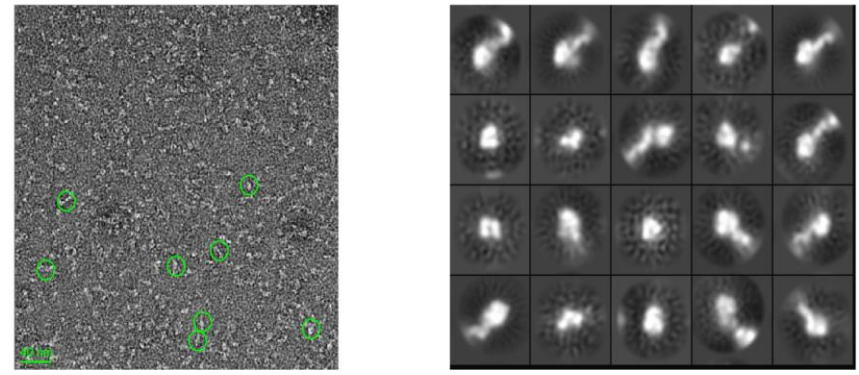

**Supplementary Figure 7. Sequence and structural analyses of the DENV NS5 – hSTAT2 interaction.** (a-c) Sequence conservation analysis of the ZIKV NS5 – hSTAT2 interaction using the ConSurf server [126]. The sequence conservation of hSTAT2 and ZIKV NS5 residues are colored coded and mapped onto the crystal structure of ZIKV RdRP – hSTAT2 (a) and cyro-EM structure of ZIKV NS5 – hSTAT2 (b,c). (d) Sequence alignment of the NS5 proteins from members of the *Flaviviridae* family, with the identical residues colored in red and the hSTAT2-binding sites of ZIKV NS5 marked by green asterisks. (e) Representative negative-stain EM image of DENV NS5-hSTAT2$_{1\text{-}713}$. Bar: 40nm. (f) Characteristic 2D class averages with CTF correction.

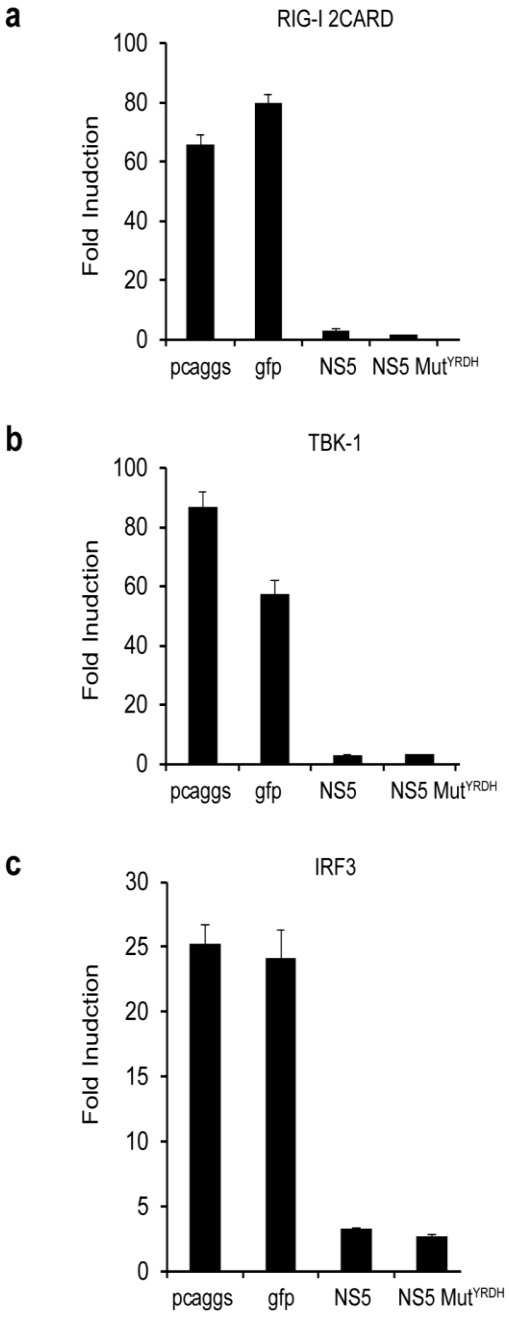


**Supplementary Figure 8. IFN-β promoter-driven luciferase activity assay.** Fold increase of interferon β production activated by RIG-2CARD (a) TBK-1 (b) and IRF3 (c) in 293T cells transfected with WT or $Mut^{YRDH}$ ZIKV NS5.

**Table 1 Crystallographic data collection and refinement statistics**

| | | ZIKV NS5 (PDB 5TMH) | ZIKV RdRp - hSTAT2$_{1-713}$ (PDB 6UX2) |
|---|---|---|---|
| **Data collection** | | | |
| Space group | | *P 2 2$_1$ 2$_1$* | *P 1 2$_1$ 1* |
| Cell dimensions | | | |
| *a*, *b*, *c* (Å) | | 95.1, 136.5, 197.0 | 85.11, 124.7, 84.78 |
| | (°) | 90, 90, 90 | 90, 109.39, 90 |
| Resolution (Å) | | 50.00-3.30 (3.42-3.30)[a] | 50.00-3.00 (3.11-3.00)[a] |
| $R_{merge}$ | | 0.31 (0.84) | 0.126 (0.696) |
| *I*/ (*I*) | | 5.30 (1.70) | 10.26 (1.67) |
| $CC_{1/2}$ | | 0.979 (0.748) | 0.996 (0.813) |
| Completeness (%) | | 99.40 (97.10) | 97.86 (83.07) |
| Redundancy | | 6.2 (5.7) | 6.0 (5.0) |
| **Refinement** | | | |
| Resolution (Å) | | 48.30-3.28 (3.36-3.28) | 49.24-3.01 (3.12-3.01) |
| No. reflections | | 39405 (3511) | 32543 (2733) |
| $R_{work}$ / $R_{free}$ | | 26.2/29.3 (34.4/40.5) | 24.2/26.4 (35.6/37.8) |
| No. atoms | | | |
| Protein | | 13391 | 9260 |
| Ligand/ion | | 38 | 22 |
| Water | | | 83 |
| *B* factors | | | |
| Protein | | 54.12 | 69.82 |
| Ligand/ion | | 68.85 | 89.00 |
| Water | | | 56.40 |
| R.m.s. deviations | | | |
| Bond lengths (Å) | | 0.002 | 0.006 |
| Bond angles (°) | | 0.55 | 1.00 |

[a]Values in parentheses are for highest-resolution shell.

**Table 2 Statistics of cryo-EM structure determination of the full-length ZIKV NS5 - hSTAT2$_{1\text{-}713}$ complex**

| | ZIKV NS5 – hSTAT2 $_{1\text{-}713}$ |
|---|---|
| **Cryo-EM data collection and processing** | |
| Voltage (kV) | 300 |
| Microscope | Krios |
| Camera | K2 summit |
| Magnification | x130,000 |
| Pixel size (Å) | 1.07 |
| Frame exposure time (s) | 0.2 |
| Number of frames/movie | 40 |
| Total electron dose (e-/Å$^2$) | 48 |
| Particle defocus range (μm) | 1.0-3.0 |
| Number of movies | 1,762 |
| Number of particles for final map | 118,760 |
| Symmetry for final maps | C1 |
| Resolution (Å) | 4.0 |
| Map sharpening B-factor (Å$^2$) | -167 |
| **Atomic model refinement** | |
| Number of protein residues | 1,231 |
| Number of atoms | 9,893 |
| RMSD bond lengths (Å) | 0.01 |
| RMSD bond angles ( ) | 1.01 |
| MolProbity score | 2.55 |
| Clash score | 13.59 |
| Rotamer outliers (%) | 0.85 |
| Ramachandran statistics | |
| Favored (%) | 90.99 |
| Allowed (%) | 9.01 |
| Outliers (%) | 0 |

## Reference


1 Moore, C. G. *et al.* Aedes aegypti in Puerto Rico: environmental determinants of larval abundance and relation to dengue virus transmission. *The American journal of tropical medicine and hygiene* **27**, 1225-1231, doi:10.4269/ajtmh.1978.27.1225 (1978).

2 Klema, V. J., Padmanabhan, R. & Choi, K. H. Flaviviral Replication Complex: Coordination between RNA Synthesis and 5'-RNA Capping. *Viruses* **7**, 4640-4656, doi:10.3390/v7082837 (2015).

3 Mazeaud, C., Freppel, W. & Chatel-Chaix, L. The Multiples Fates of the Flavivirus RNA Genome During Pathogenesis. *Frontiers in genetics* **9**, 595, doi:10.3389/fgene.2018.00595 (2018).

4 Ackermann, M. & Padmanabhan, R. De novo synthesis of RNA by the dengue virus RNA-dependent RNA polymerase exhibits temperature dependence at the initiation but not elongation phase. *The Journal of biological chemistry* **276**, 39926-39937, doi:10.1074/jbc.M104248200 (2001).

5 Bressanelli, S., Tomei, L., Rey, F. A. & De Francesco, R. Structural analysis of the hepatitis C virus RNA polymerase in complex with ribonucleotides. *Journal of virology* **76**, 3482-3492, doi:10.1128/jvi.76.7.3482-3492.2002 (2002).

6 Kao, C. C., Singh, P. & Ecker, D. J. De novo initiation of viral RNA-dependent RNA synthesis. *Virology* **287**, 251-260, doi:10.1006/viro.2001.1039 (2001).

7 Selisko, B. *et al.* Molecular basis for nucleotide conservation at the ends of the dengue virus genome. *PLoS pathogens* **8**, e1002912, doi:10.1371/journal.ppat.1002912 (2012).

8 Selisko, B., Wang, C., Harris, E. & Canard, B. Regulation of Flavivirus RNA synthesis and replication. *Current opinion in virology* **9**, 74-83, doi:10.1016/j.coviro.2014.09.011 (2014).

9 Appleby, T. C. *et al.* Viral replication. Structural basis for RNA replication by the hepatitis C virus polymerase. *Science* **347**, 771-775, doi:10.1126/science.1259210 (2015).

10 Caillet-Saguy, C., Lim, S. P., Shi, P. Y., Lescar, J. & Bressanelli, S. Polymerases of hepatitis C viruses and flaviviruses: structural and mechanistic insights and drug development. *Antiviral research* **105**, 8-16, doi:10.1016/j.antiviral.2014.02.006 (2014).

11 Brinton, M. A., Fernandez, A. V. & Dispoto, J. H. The 3'-nucleotides of flavivirus genomic RNA form a conserved secondary structure. *Virology* **153**, 113-121, doi:10.1016/0042-6822(86)90012-7 (1986).

12 Grange, T., Bouloy, M. & Girard, M. Stable secondary structures at the 3'-end of the genome of yellow fever virus (17 D vaccine strain). *FEBS letters* **188**, 159-163, doi:10.1016/0014-5793(85)80895-4 (1985).

13 Irie, K., Mohan, P. M., Sasaguri, Y., Putnak, R. & Padmanabhan, R. Sequence analysis of cloned dengue virus type 2 genome (New Guinea-C strain). *Gene* **75**, 197-211,

doi:10.1016/0378-1119(89)90266-7 (1989).

14 Mohan, P. M. & Padmanabhan, R. Detection of stable secondary structure at the 3' terminus of dengue virus type 2 RNA. *Gene* **108**, 185-191, doi:10.1016/0378-1119(91)90433-c (1991).

15 Yu, L. & Markoff, L. The topology of bulges in the long stem of the flavivirus 3' stem-loop is a major determinant of RNA replication competence. *Journal of virology* **79**, 2309-2324, doi:10.1128/JVI.79.4.2309-2324.2005 (2005).

16 Blackwell, J. L. & Brinton, M. A. BHK cell proteins that bind to the 3' stem-loop structure of the West Nile virus genome RNA. *Journal of virology* **69**, 5650-5658 (1995).

17 Blackwell, J. L. & Brinton, M. A. Translation elongation factor-1 alpha interacts with the 3' stem-loop region of West Nile virus genomic RNA. *Journal of virology* **71**, 6433-6444 (1997).

18 Chen, C. J. *et al.* RNA-protein interactions: involvement of NS3, NS5, and 3' noncoding regions of Japanese encephalitis virus genomic RNA. *Journal of virology* **71**, 3466-3473 (1997).

19 Brinton, M. A. & Dispoto, J. H. Sequence and secondary structure analysis of the 5'-terminal region of flavivirus genome RNA. *Virology* **162**, 290-299, doi:10.1016/0042-6822(88)90468-0 (1988).

20 Cahour, A., Pletnev, A., Vazielle-Falcoz, M., Rosen, L. & Lai, C. J. Growth-restricted dengue virus mutants containing deletions in the 5' noncoding region of the RNA genome. *Virology* **207**, 68-76, doi:10.1006/viro.1995.1052 (1995).

21 Filomatori, C. V., Iglesias, N. G., Villordo, S. M., Alvarez, D. E. & Gamarnik, A. V. RNA sequences and structures required for the recruitment and activity of the dengue virus polymerase. *The Journal of biological chemistry* **286**, 6929-6939, doi:10.1074/jbc.M110.162289 (2011).

22 Villordo, S. M., Carballeda, J. M., Filomatori, C. V. & Gamarnik, A. V. RNA Structure Duplications and Flavivirus Host Adaptation. *Trends in microbiology* **24**, 270-283, doi:10.1016/j.tim.2016.01.002 (2016).

23 Alvarez, D. E., Filomatori, C. V. & Gamarnik, A. V. Functional analysis of dengue virus cyclization sequences located at the 5' and 3'UTRs. *Virology* **375**, 223-235, doi:10.1016/j.virol.2008.01.014 (2008).

24 Zhang, B., Dong, H., Stein, D. A., Iversen, P. L. & Shi, P. Y. West Nile virus genome cyclization and RNA replication require two pairs of long-distance RNA interactions. *Virology* **373**, 1-13, doi:10.1016/j.virol.2008.01.016 (2008).

25 Liu, L. *et al.* Flavivirus RNA cap methyltransferase: structure, function, and inhibition. *Frontiers in biology* **5**, 286-303, doi:10.1007/s11515-010-0660-y (2010).

26 Warrener, P., Tamura, J. K. & Collett, M. S. RNA-stimulated NTPase activity associated with yellow

fever virus NS3 protein expressed in bacteria. *Journal of virology* **67**, 989-996 (1993).

27 Kuo, M. D. *et al.* Characterization of the NTPase activity of Japanese encephalitis virus NS3 protein. *The Journal of general virology* **77 ( Pt 9)**, 2077-2084, doi:10.1099/0022-1317-77-9-2077 (1996).

28 Bollati, M. *et al.* Recognition of RNA cap in the Wesselsbron virus NS5 methyltransferase domain: implications for RNA-capping mechanisms in Flavivirus. *Journal of molecular biology* **385**, 140-152, doi:10.1016/j.jmb.2008.10.028 (2009).

29 Issur, M. *et al.* The flavivirus NS5 protein is a true RNA guanylyltransferase that catalyzes a two-step reaction to form the RNA cap structure. *Rna* **15**, 2340-2350, doi:10.1261/rna.1609709 (2009).

30 Ray, D. *et al.* West Nile virus 5'-cap structure is formed by sequential guanine N-7 and ribose 2'-O methylations by nonstructural protein 5. *Journal of virology* **80**, 8362-8370, doi:10.1128/JVI.00814-06 (2006).

31 Zhou, Y. *et al.* Structure and function of flavivirus NS5 methyltransferase. *Journal of virology* **81**, 3891-3903, doi:10.1128/JVI.02704-06 (2007).

32 Egloff, M. P., Benarroch, D., Selisko, B., Romette, J. L. & Canard, B. An RNA cap (nucleoside-2'-O-)-methyltransferase in the flavivirus RNA polymerase NS5: crystal structure and functional characterization. *The EMBO journal* **21**, 2757-2768, doi:10.1093/emboj/21.11.2757 (2002).

33 Dong, H., Ren, S., Li, H. & Shi, P. Y. Separate molecules of West Nile virus methyltransferase can independently catalyze the N7 and 2'-O methylations of viral RNA cap. *Virology* **377**, 1-6, doi:10.1016/j.virol.2008.04.026 (2008).

34 Zhao, Y. *et al.* Molecular basis for specific viral RNA recognition and 2'-O-ribose methylation by the dengue virus nonstructural protein 5 (NS5). *Proceedings of the National Academy of Sciences of the United States of America* **112**, 14834-14839, doi:10.1073/pnas.1514978112 (2015).

35 Potisopon, S. *et al.* The methyltransferase domain of dengue virus protein NS5 ensures efficient RNA synthesis initiation and elongation by the polymerase domain. *Nucleic acids research* **42**, 11642-11656, doi:10.1093/nar/gku666 (2014).

36 Dong, H. *et al.* 2'-O methylation of internal adenosine by flavivirus NS5 methyltransferase. *PLoS pathogens* **8**, e1002642, doi:10.1371/journal.ppat.1002642 (2012).

37 Lu, G. & Gong, P. Crystal Structure of the full-length Japanese encephalitis virus NS5 reveals a conserved methyltransferase-polymerase interface. *PLoS pathogens* **9**, e1003549, doi:10.1371/journal.ppat.1003549 (2013).

38 El Sahili, A. *et al.* NS5 from Dengue Virus Serotype 2 Can Adopt a Conformation Analogous to That of Its Zika Virus and Japanese Encephalitis Virus Homologues. *Journal of virology* **94**, doi:10.1128/JVI.01294-19 (2019).

39 Lim, S. P. *et al.* Potent Allosteric Dengue Virus NS5 Polymerase Inhibitors: Mechanism of Action and Resistance Profiling. *PLoS pathogens* **12**, e1005737, doi:10.1371/journal.ppat.1005737 (2016).

40 Zhao, Y. *et al.* A crystal structure of the Dengue virus NS5 protein reveals a novel inter-domain interface essential for protein flexibility and virus replication. *PLoS pathogens* **11**, e1004682, doi:10.1371/journal.ppat.1004682 (2015).

41 Bussetta, C. & Choi, K. H. Dengue virus nonstructural protein 5 adopts multiple conformations in solution. *Biochemistry* **51**, 5921-5931, doi:10.1021/bi300406n (2012).

42 Kapoor, M. *et al.* Association between NS3 and NS5 proteins of dengue virus type 2 in the putative RNA replicase is linked to differential phosphorylation of NS5. *The Journal of biological chemistry* **270**, 19100-19106, doi:10.1074/jbc.270.32.19100 (1995).

43 Moreland, N. J. *et al.* Monoclonal antibodies against dengue NS2B and NS3 proteins for the study of protein interactions in the flaviviral replication complex. *J Virol Methods* **179**, 97-103, doi:10.1016/j.jviromet.2011.10.006 (2012).

44 Yu, L., Takeda, K. & Markoff, L. Protein-protein interactions among West Nile non-structural proteins and transmembrane complex formation in mammalian cells. *Virology* **446**, 365-377, doi:10.1016/j.virol.2013.08.006 (2013).

45 Takahashi, H. *et al.* Establishment of a robust dengue virus NS3-NS5 binding assay for identification of protein-protein interaction inhibitors. *Antiviral research* **96**, 305-314, doi:10.1016/j.antiviral.2012.09.023 (2012).

46 Yon, C. *et al.* Modulation of the nucleoside triphosphatase/RNA helicase and 5'-RNA triphosphatase activities of Dengue virus type 2 nonstructural protein 3 (NS3) by interaction with NS5, the RNA-dependent RNA polymerase. *The Journal of biological chemistry* **280**, 27412-27419, doi:10.1074/jbc.M501393200 (2005).

47 Xu, S. *et al.* Zika virus NS3 is a canonical RNA helicase stimulated by NS5 RNA polymerase. *Nucleic acids research* **47**, 8693-8707, doi:10.1093/nar/gkz650 (2019).

48 Johansson, M., Brooks, A. J., Jans, D. A. & Vasudevan, S. G. A small region of the dengue virus-encoded RNA-dependent RNA polymerase, NS5, confers interaction with both the nuclear transport receptor importin-ss and the viral helicase, NS3. *Journal Of General Virology* **82**, 735-745, doi:Doi 10.1099/0022-1317-82-4-735 (2001).

49 Tay, M. Y. F. *et al.* The C-terminal 50 Amino Acid Residues of Dengue NS3 Protein Are Important for NS3-NS5 Interaction and Viral Replication. *Journal Of Biological Chemistry* **290**, 2379-2394, doi:10.1074/jbc.M114.607341 (2015).

50 Lester, S. N. & Li, K. Toll-Like Receptors in Antiviral Innate Immunity. *Journal of molecular biology*

**426**, 1246-1264, doi:10.1016/j.jmb.2013.11.024 (2014).

51 Akira, S. TLR signaling. *Current topics in microbiology and immunology* **311**, 1-16, doi:10.1007/3-540-32636-7_1 (2006).

52 Patel, J. R. & Garcia-Sastre, A. Activation and regulation of pathogen sensor RIG-I. *Cytokine Growth F R* **25**, 513-523, doi:10.1016/j.cytogfr.2014.08.005 (2014).

53 Kato, H., Takahasi, K. & Fujita, T. RIG-I-like receptors: cytoplasmic sensors for non-self RNA. *Immunol Rev* **243**, 91-98, doi:10.1111/j.1600-065X.2011.01052.x (2011).

54 Goubau, D., Deddouche, S. & Reis e Sousa, C. Cytosolic sensing of viruses. *Immunity* **38**, 855-869, doi:10.1016/j.immuni.2013.05.007 (2013).

55 Paludan, S. R. & Bowie, A. G. Immune sensing of DNA. *Immunity* **38**, 870-880, doi:10.1016/j.immuni.2013.05.004 (2013).

56 Kato, H. *et al.* Differential roles of MDA5 and RIG-I helicases in the recognition of RNA viruses. *Nature* **441**, 101-105, doi:10.1038/nature04734 (2006).

57 Fredericksen, B. L., Keller, B. C., Fornek, J., Katze, M. G. & Gale, M. Establishment and maintenance of the innate antiviral response to west nile virus involves both RIG-I and MDA5 signaling through IPS-1. *Journal of virology* **82**, 609-616, doi:10.1128/Jvi.01305-07 (2008).

58 Loo, Y. M. *et al.* Distinct RIG-I and MDA5 signaling by RNA viruses in innate immunity. *Journal of virology* **82**, 335-345, doi:10.1128/Jvi.01080-07 (2008).

59 Fredericksen, B. L. & Gale, M. West Nile virus evades activation of interferon regulatory factor 3 through RIG-I-dependent and -independent pathways without antagonizing host defense signaling. *Journal of virology* **80**, 2913-2923, doi:10.1128/Jvi.80.6.2913-2923.2006 (2006).

60 Miorin, L., Maestre, A. M., Fernandez-Sesma, A. & Garcia-Sastre, A. Antagonism of type I interferon by flaviviruses. *Biochem Bioph Res Co* **492**, 587-596, doi:10.1016/j.bbrc.2017.05.146 (2017).

61 Aguirre, S. *et al.* Dengue virus NS2B protein targets cGAS for degradation and prevents mitochondrial DNA sensing during infection. *Nat Microbiol* **2**, doi:Artn 17037 10.1038/Nmicrobiol.2017.37 (2017).

62 Aguirre, S. *et al.* DENV Inhibits Type I IFN Production in Infected Cells by Cleaving Human STING. *PLoS pathogens* **8**, doi:ARTN e1002934 10.1371/journal.ppat.1002934 (2012).

63 Ivashkiv, L. B. & Donlin, L. T. Regulation of type I interferon responses. *Nat Rev Immunol* **14**, 36-49, doi:10.1038/nri3581 (2014).

64 Levy, D. E. & Darnell, J. E. STATs: Transcriptional control and biological impact. *Nat Rev Mol Cell Bio* **3**, 651-662, doi:10.1038/nrm909 (2002).

65 Best, S. M. The Many Faces of the Flavivirus NS5 Protein in Antagonism of Type I Interferon Signaling. *Journal of virology* **91**, doi:UNSP e01970 10.1128/JVI.01970-16 (2017).

66 Gough, D. J., Messina, N. L., Clarke, C. J. P., Johnstone, R. W. & Levy, D. E. Constitutive Type I Interferon Modulates Homeostatic Balance through Tonic Signaling. *Immunity* **36**, 166-174, doi:10.1016/j.immuni.2012.01.011 (2012).

67 Mostafavi, S. *et al.* Parsing the Interferon Transcriptional Network and Its Disease Associations. *Cell* **164**, 564-578, doi:10.1016/j.cell.2015.12.032 (2016).

68 Platanitis, E. *et al.* A molecular switch from STAT2-IRF9 to ISGF3 underlies interferon-induced gene transcription. *Nat Commun* **10**, doi:Artn 292110.1038/S41467-019-10970-Y (2019).

69 Blaszczyk, K. *et al.* The unique role of STAT2 in constitutive and IFN-induced transcription and antiviral responses. *Cytokine Growth F R* **29**, 71-81, doi:10.1016/j.cytogfr.2016.02.010 (2016).

70 Melen, K., Kinnunen, L. & Julkunen, I. Arginine/lysine-rich structural element is involved in interferon-induced nuclear import of STATs. *Journal Of Biological Chemistry* **276**, 16447-16455, doi:DOI 10.1074/jbc.M008821200 (2001).

71 Fagerlund, R., Melen, K., Kinnunen, L. & Julkunen, I. Arginine/lysine-rich nuclear localization signals mediate interactions between dimeric STATs and importin alpha 5. *Journal Of Biological Chemistry* **277**, 30072-30078, doi:10.1074/jbc.M202943200 (2002).

72 Melen, K. *et al.* Importin alpha nuclear localization signal binding sites for STAT1, STAT2, and influenza a virus nucleoprotein. *Journal Of Biological Chemistry* **278**, 28193-28200, doi:10.1074/jbc.M303571200 (2003).

73 Banninger, G. & Reich, N. C. STAT2 nuclear trafficking. *Journal Of Biological Chemistry* **279**, 39199-39206, doi:10.1074/jbc.M400815200 (2004).

74 Zust, R. *et al.* Type I Interferon Signals in Macrophages and Dendritic Cells Control Dengue Virus Infection: Implications for a New Mouse Model To Test Dengue Vaccines. *Journal of virology* **88**, 7276-7285, doi:10.1128/Jvi.03827-13 (2014).

75 Lazear, H. M. *et al.* A Mouse Model of Zika Virus Pathogenesis. *Cell Host Microbe* **19**, 720-730, doi:10.1016/j.chom.2016.03.010 (2016).

76 Rossi, S. L. *et al.* Characterization of a Novel Murine Model to Study Zika Virus. *American Journal Of Tropical Medicine And Hygiene* **94**, 1362-1369, doi:10.4269/ajtmh.16-0111 (2016).

77 Aliota, M. T. *et al.* Characterization of Lethal Zika Virus Infection in AG129 Mice. *Plos Neglect Trop D* **10**, doi:ARTN e0004682 10.1371/journal.pntd.0004682 (2016).

78 Ashour, J., Laurent-Rolle, M., Shi, P. Y. & Garcia-Sastre, A. NS5 of Dengue Virus Mediates STAT2

Binding and Degradation. *Journal of virology* **83**, 5408-5418, doi:10.1128/Jvi.02188-08 (2009).

79 Jones, M. *et al.* Dengue virus inhibits alpha interferon signaling by reducing STAT2 expression. *Journal of virology* **79**, 5414-5420, doi:10.1128/Jvi.79.9.5414-5420.2005 (2005).

80 Morrison, J. *et al.* Dengue Virus Co-opts UBR4 to Degrade STAT2 and Antagonize Type I Interferon Signaling. *PLoS pathogens* **9**, doi:ARTN e1003265 10.1371/journal.ppat.1003265 (2013).

81 Grant, A. *et al.* Zika Virus Targets Human STAT2 to Inhibit Type I Interferon Signaling. *Cell Host Microbe* **19**, 882-890, doi:10.1016/j.chom.2016.05.009 (2016).

82 Chaudhary, V. *et al.* Selective Activation of Type II Interferon Signaling by Zika Virus NS5 Protein. *Journal of virology* **91**, doi:UNSP e00163 10.1128/JVI.00163-17 (2017).

83 Laurent-Rolle, M. *et al.* The Interferon Signaling Antagonist Function of Yellow Fever Virus NS5 Protein Is Activated by Type I Interferon. *Cell Host Microbe* **16**, 314-327, doi:10.1016/j.chom.2014.07.015 (2014).

84 Lin, R. J., Chang, B. L., Yu, H. P., Liao, C. L. & Lin, Y. L. Blocking of interferon-induced Jak-Stat signaling by Japanese encephalitis virus NS5 through a protein tyrosine phosphatase-mediated mechanism. *Journal of virology* **80**, 5908-5918, doi:10.1128/Jvi.02714-05 (2006).

85 Mazzon, M., Jones, M., Davidson, A., Chain, B. & Jacobs, M. Dengue Virus NS5 Inhibits Interferon-alpha Signaling by Blocking Signal Transducer and Activator of Transcription 2 Phosphorylation. *J Infect Dis* **200**, 1261-1270, doi:10.1086/605847 (2009).

86 Laurent-Rolle, M. *et al.* The NS5 Protein of the Virulent West Nile Virus NY99 Strain Is a Potent Antagonist of Type I Interferon-Mediated JAK-STAT Signaling. *Journal of virology* **84**, 3503-3515, doi:10.1128/Jvi.01161-09 (2010).

87 Brooks, A. J. *et al.* The interdomain region of dengue NS5 protein that binds to the viral helicase NS3 contains independently functional importin beta 1 and importin alpha/beta-recognized nuclear localization signals. *Journal Of Biological Chemistry* **277**, 36399-36407, doi:10.1074/jbc.M204977200 (2002).

88 Forwood, J. K. *et al.* The 37-amino-acid interdomain of dengue virus NS5 protein contains a functional NLS and inhibitory CK2 site. *Biochem Bioph Res Co* **257**, 731-737, doi:DOI 10.1006/bbrc.1999.0370 (1999).

89 Hannemann, H. *et al.* Serotype-specific Differences in Dengue Virus Non-structural Protein 5 Nuclear Localization. *Journal Of Biological Chemistry* **288**, 22621-22635, doi:10.1074/jbc.M113.481382 (2013).

90 Tay, M. Y. *et al.* Nuclear localization of dengue virus (DENV) 1-4 non-structural protein 5; protection against all 4 DENV serotypes by the inhibitor Ivermectin. *Antiviral research* **99**, 301-306,

doi:10.1016/j.antiviral.2013.06.002 (2013).

91 Tay, M. Y. *et al.* The C-terminal 18 Amino Acid Region of Dengue Virus NS5 Regulates its Subcellular Localization and Contains a Conserved Arginine Residue Essential for Infectious Virus Production. *PLoS pathogens* **12**, e1005886, doi:10.1371/journal.ppat.1005886 (2016).

92 De Maio, F. A. *et al.* The Dengue Virus NS5 Protein Intrudes in the Cellular Spliceosome and Modulates Splicing. *PLoS pathogens* **12**, e1005841, doi:10.1371/journal.ppat.1005841 (2016).

93 Ng, I. H. W. *et al.* Zika Virus NS5 Forms Supramolecular Nuclear Bodies That Sequester Importin-alpha and Modulate the Host Immune and Pro-Inflammatory Response in Neuronal Cells. *Acs Infect Dis* **5**, 932-948, doi:10.1021/acsinfecdis.8b00373 (2019).

94 Murakami, E. *et al.* Mechanism of Activation of PSI-7851 and Its Diastereoisomer PSI-7977. *Journal Of Biological Chemistry* **285**, 34337-34347, doi:10.1074/jbc.M110.161802 (2010).

95 Sofia, M. J. *et al.* Discovery of a beta-d-2'-deoxy-2'-alpha-fluoro-2'-beta-C-methyluridine nucleotide prodrug (PSI-7977) for the treatment of hepatitis C virus. *Journal of medicinal chemistry* **53**, 7202-7218, doi:10.1021/jm100863x (2010).

96 Ferreira, A. C. *et al.* Sofosbuvir protects Zika virus-infected mice from mortality, preventing short- and long-term sequelae. *Scientific reports* **7**, 9409, doi:10.1038/s41598-017-09797-8 (2017).

97 Yokokawa, F. *et al.* Discovery of Potent Non-Nucleoside Inhibitors of Dengue Viral RNA-Dependent RNA Polymerase from a Fragment Hit Using Structure-Based Drug Design. *Journal of medicinal chemistry* **59**, 3935-3952, doi:10.1021/acs.jmedchem.6b00143 (2016).

98 Heinz, F. X. & Stiasny, K. Flaviviruses and flavivirus vaccines. *Vaccine* **30**, 4301-4306, doi:10.1016/j.vaccine.2011.09.114 (2012).

99 Barrett, A. D. & Teuwen, D. E. Yellow fever vaccine - how does it work and why do rare cases of serious adverse events take place? *Current opinion in immunology* **21**, 308-313, doi:10.1016/j.coi.2009.05.018 (2009).

100 Otwinowski, Z. & Minor, W. Processing of X-ray diffraction data collected in oscillation mode. *Method Enzymol* **276**, 307-326, doi:Doi 10.1016/S0076-6879(97)76066-X (1997).

101 Mccoy, A. J. *et al.* Phaser crystallographic software. *J Appl Crystallogr* **40**, 658-674, doi:10.1107/S0021889807021206 (2007).

102 Emsley, P. & Cowtan, K. Coot: model-building tools for molecular graphics. *Acta Crystallogr D Biol Crystallogr* **60**, 2126-2132, doi:S0907444904019158 [pii] 10.1107/S0907444904019158 (2004).

103 Adams, P. D. *et al.* PHENIX: building new software for automated crystallographic structure determination. *Acta Crystallogr D Biol Crystallogr* **58**, 1948-1954, doi:S0907444902016657 [pii]

(2002).

104 Suloway, C. *et al.* Automated molecular microscopy: the new Leginon system. *Journal of structural biology* **151**, 41-60, doi:10.1016/j.jsb.2005.03.010 (2005).

105 Zheng, S. Q. *et al.* MotionCor2: anisotropic correction of beam-induced motion for improved cryo-electron microscopy. *Nature methods* **14**, 331-332, doi:10.1038/nmeth.4193 (2017).

106 Zhang, K. Gctf: Real-time CTF determination and correction. *Journal of structural biology* **193**, 1-12, doi:10.1016/j.jsb.2015.11.003 (2016).

107 Scheres, S. H. RELION: implementation of a Bayesian approach to cryo-EM structure determination. *Journal of structural biology* **180**, 519-530, doi:10.1016/j.jsb.2012.09.006 (2012).

108 Scheres, S. H. A Bayesian view on cryo-EM structure determination. *Journal of molecular biology* **415**, 406-418, doi:10.1016/j.jmb.2011.11.010 (2012).

109 Punjani, A., Rubinstein, J. L., Fleet, D. J. & Brubaker, M. A. cryoSPARC: algorithms for rapid unsupervised cryo-EM structure determination. *Nature methods* **14**, 290-296, doi:10.1038/nmeth.4169 (2017).

110 Vilas, J. L. *et al.* MonoRes: Automatic and Accurate Estimation of Local Resolution for Electron Microscopy Maps. *Structure* **26**, 337-344 e334, doi:10.1016/j.str.2017.12.018 (2018).

111 Pettersen, E. F. *et al.* UCSF chimera - A visualization system for exploratory research and analysis. *J Comput Chem* **25**, 1605-1612, doi:10.1002/jcc.20084 (2004).

112 Schwarz, M. C. *et al.* Rescue of the 1947 Zika Virus Prototype Strain with a Cytomegalovirus Promoter-Driven cDNA Clone. *mSphere* **1**, doi:10.1128/mSphere.00246-16 (2016).

113 Chen, X. M. *et al.* Crystal structure of a tyrosine phosphorylated STAT-1 dimer bound to DNA. *Cell* **93**, 827-839, doi:Doi 10.1016/S0092-8674(00)81443-9 (1998).

114 Mao, X. *et al.* Structural bases of unphosphorylated STAT1 association and receptor binding. *Mol Cell* **17**, 761-771, doi:10.1016/j.molcel.2005.02.021 (2005).

115 Becker, S., Groner, B. & Muller, C. W. Three-dimensional structure of the Stat3 beta homodimer bound to DNA. *Nature* **394**, 145-151, doi:Doi 10.1038/28101 (1998).

116 Neculai, D. *et al.* Structure of the unphosphorylated STAT5a dimer. *J Biol Chem* **280**, 40782-40787, doi:DOI 10.1074/jbc.M507682200 (2005).

117 Li, J. *et al.* Structural basis for DNA recognition by STAT6. *P Natl Acad Sci USA* **113**, 13015-13020, doi:10.1073/pnas.1611228113 (2016).

118 Uchil, P. D., Kumar, A. V. A. & Satchidanandam, V. Nuclear localization of flavivirus RNA synthesis

in infected cells. *J Virol* **80**, 5451-5464, doi:10.1128/Jvi.01982-05 (2006).

119 Rengachari, S. *et al.* Structural basis of STAT2 recognition by IRF9 reveals molecular insights into ISGF3 function. *Proceedings of the National Academy of Sciences of the United States of America* **115**, E601-E609, doi:10.1073/pnas.1718426115 (2018).

120 Speer, S. D. *et al.* ISG15 deficiency and increased viral resistance in humans but not mice. *Nat Commun* **7**, 11496, doi:10.1038/ncomms11496 (2016).

121 Xia, H. *et al.* An evolutionary NS1 mutation enhances Zika virus evasion of host interferon induction. *Nature communications* **9**, 414, doi:10.1038/s41467-017-02816-2 (2018).

122 Hertzog, J. *et al.* Infection with a Brazilian isolate of Zika virus generates RIG-I stimulatory RNA and the viral NS5 protein blocks type I IFN induction and signaling. *European journal of immunology* **48**, 1120-1136, doi:10.1002/eji.201847483 (2018).

123 Kumar, A. *et al.* Zika virus inhibits type-I interferon production and downstream signaling. *EMBO reports* **17**, 1766-1775, doi:10.15252/embr.201642627 (2016).

124 Grant, A. *et al.* Zika Virus Targets Human STAT2 to Inhibit Type I Interferon Signaling. *Cell host & microbe* **19**, 882-890, doi:10.1016/j.chom.2016.05.009 (2016).

125 Emeny, J. M. & Morgan, M. J. Regulation of the interferon system: evidence that Vero cells have a genetic defect in interferon production. *J Gen Virol* **43**, 247-252, doi:10.1099/0022-1317-43-1-247 (1979).

126 Ashkenazy, H. *et al.* ConSurf 2016: an improved methodology to estimate and visualize evolutionary conservation in macromolecules. *Nucleic Acids Res* **44**, W344-350, doi:10.1093/nar/gkw408 (2016).